



Publication Year	2016
Acceptance in OA @INAF	2021-04-23T13:41:06Z
Title	Electromagnetic Emission from Long-lived Binary Neutron Star Merger Remnants. II. Lightcurves and Spectra
Authors	Siegel, Daniel M.; CIOLFI, RICCARDO
DOI	10.3847/0004-637X/819/1/15
Handle	http://hdl.handle.net/20.500.12386/30884
Journal	THE ASTROPHYSICAL JOURNAL
Number	819



ELECTROMAGNETIC EMISSION FROM LONG-LIVED BINARY NEUTRON STAR MERGER REMNANTS. II. LIGHT CURVES AND SPECTRA

DANIEL M. SIEGEL¹ AND RICCARDO CIOLFI^{2,3}

¹ Max Planck Institute for Gravitational Physics (Albert Einstein Institute), Am Mühlenberg 1, D-14476 Potsdam-Golm, Germany; daniel.siegel@aei.mpg.de

² Physics Department, University of Trento, Via Sommarive 14, I-38123 Trento, Italy; riccardo.ciolfi@unitn.it

³ INFN-TIFPA, Trento Institute for Fundamental Physics and Applications, Via Sommarive 14, I-38123 Trento, Italy

Received 2015 September 3; accepted 2015 December 14; published 2016 February 24

ABSTRACT

Recent observations indicate that in a large fraction of binary neutron star (BNS) mergers a long-lived neutron star (NS) may be formed rather than a black hole. Unambiguous electromagnetic (EM) signatures of such a scenario would strongly impact our knowledge on how short gamma-ray bursts (SGRBs) and their afterglow radiation are generated. Furthermore, such EM signals would have profound implications for multimessenger astronomy with joint EM and gravitational-wave (GW) observations of BNS mergers, which will soon become reality thanks to the ground-based advanced LIGO/Virgo GW detector network. Here we explore such EM signatures based on the model presented in a companion paper, which provides a self-consistent evolution of the post-merger system and its EM emission up to $\sim 10^7$ s. Light curves and spectra are computed for a wide range of post-merger physical properties. We present X-ray afterglow light curves corresponding to the “standard” and the “time-reversal” scenario for SGRBs (prompt emission associated with the merger or with the collapse of the long-lived NS). The light curve morphologies include single and two-plateau features with timescales and luminosities that are in good agreement with *Swift* observations. Furthermore, we compute the X-ray signal that should precede the SGRB in the time-reversal scenario, the detection of which would represent smoking-gun evidence for this scenario. Finally, we find a bright, highly isotropic EM transient peaking in the X-ray band at $\sim 10^2$ – 10^4 s after the BNS merger with luminosities of $L_X \sim 10^{46}$ – 10^{48} erg s⁻¹. This signal represents a very promising EM counterpart to the GW emission from BNS mergers.

Key words: gamma-ray burst: general – gravitational waves – pulsars: general – stars: magnetars – stars: neutron – X-rays: general

1. INTRODUCTION

Merging binary neutron stars (BNSs) and neutron star–black hole (NS–BH) binaries are considered the leading scenario to explain the phenomenology of short gamma-ray bursts (SGRBs; e.g., Paczynski 1986; Eichler et al. 1989; Narayan et al. 1992; Barthelmy et al. 2005a; Fox et al. 2005; Gehrels et al. 2005; Shibata et al. 2006; Rezzolla et al. 2011; Berger et al. 2013; Tanvir et al. 2013; Paschalidis et al. 2015; Yang et al. 2015). The standard paradigm for the generation of the SGRB is an accretion powered jet from a remnant BH–torus system that is formed $\lesssim 10$ – 100 ms after merger (e.g., Narayan et al. 1992; Janka et al. 1999; Rezzolla et al. 2011; Paschalidis et al. 2015). According to this paradigm, energy release should cease once the torus has been accreted on a timescale of $\lesssim 1$ s, which is consistent with the duration of the SGRB prompt emission of less than ≈ 2 s.

However, observations by the *Swift* satellite (Gehrels et al. 2004) have recently revealed long-lasting ($\sim 10^2$ – 10^5 s), X-ray afterglows in a large fraction of SGRB events that are indicative of continuous energy release from a central engine on timescales orders of magnitude larger than the typical torus accretion timescale (up to $\sim 10^4$ s; e.g., Rowlinson et al. 2010, 2013; Gompertz et al. 2013, 2014; Lü et al. 2015). These afterglows are difficult to explain by accretion of the torus or by prolonged afterglow radiation generated by the interaction of the jet with the ambient medium (Kumar & Zhang 2015 and references therein).

If a large fraction of BNS mergers result in the formation of a stable or long-lived NS rather than a BH, extraction of rotational energy via magnetic spin-down from such an object

(typically a millisecond magnetar) could power the observed long-lasting afterglows (e.g., Zhang & Mészáros 2001; Metzger et al. 2008; Bucciantini et al. 2012; Gompertz et al. 2013; Rowlinson et al. 2013; Lü et al. 2015). If true, this challenges the NS–BH progenitor scenario in a large fraction of SGRB events. The formation of a long-lived NS in a BNS merger is indeed very likely. Recent observations of massive NSs with a mass of $\approx 2 M_\odot$ together with population synthesis models indicate that the vast majority of BNS mergers should result in the formation of a long-lived NS (Lasota et al. 1996; Belczynski et al. 2008; Demorest et al. 2010; Antoniadis et al. 2013; see Section 1 of Siegel & Ciolfi 2016 for a more detailed discussion). However, such magnetar models cannot readily explain how the prompt SGRB emission should be generated. Material dynamically ejected during the merger process as well as matter ejected subsequently in neutrino and magnetically driven winds from the remnant NS and an accretion disk strongly pollute the merger site with baryons (e.g., Oechslin et al. 2007; Dessart et al. 2009; Bauswein et al. 2013; Hotokezaka et al. 2013; Metzger & Fernández 2014; Siegel et al. 2014; Kastaun & Galeazzi 2015), which severely threatens the generation of a relativistic outflow. Even if formed by an NS–torus system shortly after merger, such a jet can be choked by the surrounding material (Murguia-Berthier et al. 2014; Nagakura et al. 2014). We note that numerical simulations of the merger process have so far not shown any evidence for jet formation in this case (Giacomazzo & Perna 2013).

The recently proposed “time-reversal” scenario (Ciolfi & Siegel 2015a, 2015b; see Rezzolla & Kumar 2015 for an

alternative proposal) offers a possible solution to this problem. In this scenario, the SGRB is associated with the time of collapse of the long-lived NS, which occurs on the spin-down timescale $\sim 10^2\text{--}10^4$ s after merger. The long-lasting X-ray afterglow radiation is produced by spin-down energy extracted from the NS prior to collapse, slowly diffusing outward through the optically thick environment composed of a pulsar wind nebula (PWN) and an outer shell of previously ejected material (see Figure 1 of Siegel & Ciolfi 2016 and Figure 1 of Ciolfi & Siegel 2015b). The problem of baryon pollution is avoided here as the NS is surrounded by a baryon-free PWN at the time of collapse. However, Margalit et al. (2015) recently questioned the formation of a massive torus around the BH after the collapse of the long-lived NS and thus the formation of a jet in this case.

While the generation of the prompt SGRB emission still remains a matter of debate, in the present paper we focus on predicting X-ray afterglow light curves and spectra for both the “standard” magnetar scenario and the time-reversal scenario (i.e., assuming that the prompt burst occurs at the time of merger or at the time of collapse of the newly formed NS) employing a detailed dynamical evolution model presented in a companion paper (Siegel & Ciolfi 2016, henceforth Paper I). This model should be applicable to any BNS merger leading to the formation of a long-lived NS. It predicts the evolution of the post-merger system and its electromagnetic (EM) emission in a self-consistent way, given some initial data that can be extracted from a numerical relativity simulation tens of milliseconds after merger. It bridges the gap between the short timescales accessible to numerical simulations of the merger process and the timescales of interest for SGRB afterglow radiation. Our model evolves the post-merger system through three main evolutionary phases (see Paper I for details). During an early baryonic wind phase the surrounding of the newly formed NS is polluted with matter while differential rotation is being removed (Phase I). Once mass loss is suppressed, a pulsar atmosphere is set up that drives a strong shock through the envelope of previously ejected matter and sweeps up all the material into a thin shell (Phase II). Finally, the system is composed of a radially expanding ejecta shell that confines a PWN centered around the NS (Phase III). The NS can collapse to a BH at any time during Phase I–III, which gives rise to very different EM emission scenarios. In the present paper, we apply this model to a wide range of physically motivated post-merger systems. We investigate the possible morphologies of X-ray light curves for both the standard and the time-reversal scenario, which can be compared to observations of the *Swift* satellite. In particular, we also compute detailed predictions for the X-ray radiation expected to precede the prompt SGRB emission in the time-reversal scenario. The latter predictions can be used to search for this X-ray signal. The presence or absence of such radiation would have strong implications on how and when SGRBs are produced in BNS mergers.

EM emission from BNS mergers is also of prime importance for multimessenger astronomy. BNS mergers are the most promising source of gravitational waves (GW) for detection with interferometric detectors such as advanced LIGO and Virgo (Abadie et al. 2010; Harry et al. 2010; Accadia et al. 2011). With those detectors starting their first science runs in 2015, joint EM and GW observations will become a routine undertaking in the very near future (Singer et al. 2014). Such multimessenger astronomy can greatly enhance the

scientific output of GW and EM observations (see Section 1 of Paper I for a more detailed discussion), although the actual benefit depends on the knowledge about the EM signals to be expected in association with BNS mergers. While the prompt SGRB emission will be observable only in a very small number of events (see Section 7), (i) more isotropic EM counterparts need to be identified that are (ii) bright and (iii) long-lasting, that are produced in a (iv) high fraction of events, and that can (v) distinguish between a BNS and an NS–BH merger (see also Section 1 of Paper I). We note that a kilonova (or macronova) might be bright enough in some cases (Berger et al. 2013; Tanvir et al. 2013; Yang et al. 2015)—a near-infrared/optical transient powered by the radioactive decay of heavy nuclei synthesized in the material dynamically ejected during a BNS or NS–BH merger (Li & Paczyński 1998; Kulkarni 2005; Rosswog 2005; Metzger et al. 2010; Roberts et al. 2011; Barnes & Kasen 2013; Piran et al. 2013; Tanaka & Hotokezaka 2013). It also fulfills the remaining criteria but the last one. While in principle it might be possible to distinguish between BNS and NS–BH mergers with a kilonova observation (Tanaka et al. 2014), it is difficult in practice (Yang et al. 2015). Employing our model, we find here an EM counterpart signal of a BNS merger that fulfills all criteria (i)–(v). If observed, such an EM signature would represent compelling evidence for a BNS merger and for the formation of a long-lived NS, which, in turn, would place strong constraints on the unknown equation of state of nuclear matter at high densities. Moreover, such an EM counterpart can reveal important information about the evolution of the post-merger system and the associated physical processes not accessible to GW observations.

This paper is organized as follows. In Section 2, we define the X-ray light curves and spectra the following discussion is based on. Section 3 briefly describes the parameters of our model and assigns associated ranges that define the parameter space for post-merger configurations to be explored in the following sections. Further assumptions are also discussed. In Section 4, we present in detail the results of a typical run with fiducial parameter values and comment on the underlying physical processes. Section 5 illustrates the influence and importance of individual parameters, while Section 6 explores the entire parameter space to provide a more comprehensive overview of the different morphologies of possible X-ray light curves, which are compared to observations. Finally, Section 7 is reserved for a discussion of our numerical results in the context of X-ray afterglows of SGRBs and EM counterparts to the GW signal of the inspiral and merger of BNS systems and it presents our main conclusions. For details on the evolution model and the underlying phenomenology, we refer to Paper I.

2. LIGHT CURVES AND SPECTRA: DEFINITIONS

The most important prediction of our model to be compared to observations is the frequency and time-dependent light curve $L_{\text{obs}}(t, x)$ as seen by a distant observer (cf. Equation (138) of Paper I).⁴ Here, $x = h\nu/m_e c^2$ defines a normalized dimensionless photon energy, where ν is the photon frequency, h the Planck constant, m_e the electron mass, and c the speed of light. This light curve characterizes the radiation emerging from the

⁴ Henceforth we drop the primes used in Paper I to distinguish between lab-frame and observer quantities. We assume that their respective meanings should be clear from the context.

Table 1

Model Input Parameters (see Table 2 of Paper I for References to Explicit Definitions of these Quantities) with Corresponding Ranges Considered Here and a Fiducial Value Used for the Model Run Described in Section 4

Parameter	Range	Fiducial value	Description
\dot{M}_{in}	10^{-3} – $10^{-1} M_{\odot} \text{s}^{-1}$	$5 \times 10^{-3} M_{\odot} \text{s}^{-1}$	initial mass-loss rate of the NS
t_{dr}	0.1–10 s	1 s	timescale for removal of differential rotation from the NS
σ_M	1–2	2	ratio of t_{dr} to the timescale for decrease of the mass-loss rate
$v_{\text{ej,in}}$	0.01–0.1 c	0.01 c	initial expansion speed of the baryonic ejecta material
\bar{B}	10^{14} – 10^{17} G	10^{16} G	magnetic field strength in the outer layers of the NS
η_{B_p}	0.01–0.5	0.1	dipolar magnetic field strength of the pulsar in units of \bar{B}
$E_{\text{rot,NS,in}}$	$(1\text{--}5) \times 10^{52}$ erg	5×10^{52} erg	initial rotational energy of the NS
P_c	0.5–2 ms	0.5 ms	initial central spin period of the NS
R_e	...	11 km	equatorial radius of the NS
$M_{\text{NS,in}}$...	$2.4 M_{\odot}$	initial mass of the NS
I_{pul}	...	$2 \times 10^{45} \text{ g cm}^2$	moment of inertia of the pulsar
$T_{\text{ej,NS,in}}$	10–30 MeV	20 MeV	initial temperature of the material ejected from the NS surface ^a
κ	0.2–10 $\text{cm}^2 \text{ g}^{-1}$	$0.2 \text{ cm}^2 \text{ g}^{-1}$	opacity of the ejecta material
t_{ν}	0.3–3 s	0.3 s	neutrino-cooling timescale
η_{B_n}	10^{-4} – 10^{-2}	10^{-3}	fraction of the total pulsar wind power injected as magnetic energy per unit time into the PWN
η_{RS}	...	0.1	efficiency of converting pulsar wind power into random kinetic energy of accelerated particles in the PWN
γ_{max}	10^4 – 10^6	10^4	maximum Lorentz factor for non-thermal particle injection into the PWN
Γ_c	0.5–2.5	2.5	power-law index of the non-thermal spectrum for particle injection into the PWN
f_{coll}	0.1–3	1	(only in the collapse scenario) parameter specifying the time of collapse of the NS in units of the spin-down timescale (collapse during Phase III) or in units of t_{dr} (“ $f_{\text{coll,PI}}$ ” collapse during Phase I)

Note. Most of these parameters can be extracted from (or at least estimated/constrained using) numerical relativity simulations of BNS mergers.

^a We employ this parameter here for convenience instead of the initial specific internal energy of the NS material (see Table 2 of Paper I), assuming an ideal gas equation of state with adiabatic index of $\Gamma = 2$.

post-merger system and it is reconstructed from the numerical integration of the model evolution equations (Equations (1)–(15) of Paper I) as described in Section 5.7 of Paper I. This reconstruction takes into account the combined effects of relativistic beaming and the relativistic Doppler and time-of-flight effects. In order to facilitate a comparison with observations, we further define several luminosities restricted to specific wavelength bands, some of which correspond to the spectral ranges of the instruments aboard the *Swift* satellite (Gehrels et al. 2004):

$$L_{\text{obs,band}}(t) = \int_{X_{\text{band}}} L_{\text{obs}}(t, x) dx. \quad (1)$$

The wavelength bands we consider are as follows. $X_{\text{tot}} = [x_{\text{min}}, x_{\text{max}}]$ represents the entire spectral range considered by our model from radio to γ -ray energies, with typically $x_{\text{min}} = 10^{-18}$ and $x_{\text{max}} = \gamma_{\text{max}}$ (cf. Section 5.2 of Paper I), where γ_{max} denotes the maximum Lorentz factor of the non-thermal particles in the PWN (cf. Table 1). Moreover, $X_{\text{XRT}} = [x_{\text{min,XRT}}, x_{\text{max,XRT}}]$, $X_{\text{BAT}} = [x_{\text{min,BAT}}, x_{\text{max,BAT}}]$, and $X_{\text{UVOT}} = [x_{\text{min,UVOT}}, x_{\text{max,UVOT}}]$, with associated energy/wavelength ranges of 0.3–10 keV, 15–150 keV, and 170–650 nm, respectively, correspond to the spectral ranges of the X-Ray Telescope (XRT; Burrows et al. 2005), the Burst Alert Telescope (BAT; Barthelmy et al. 2005b), and the Ultraviolet/Optical Telescope (UVOT; Roming et al. 2005) aboard the *Swift* spacecraft. Furthermore, we define energy bands labelled as “low” and “high” that contain the radiation emitted below and above the sensitivity regimes of *Swift*. The subdivision into individual bands according to (1) allows us to

make very specific predictions for the EM emission from long-lived BNS merger remnants that falls into the sensitivity windows of the leading instruments for the observation of SGRBs and their afterglows. However, predictions for any other desired spectral range can easily be generated.

3. GENERAL INPUT PARAMETERS AND SETUP

3.1. Parameter Values

According to our model presented in Paper I, predictions for the EM emission from a BNS merger remnant result from a self-consistent numerical evolution of a set of coupled differential equations based on several input parameters, which we list in Table 1. In this paper, we explore physically plausible ranges for these parameters (see “Range” in Table 1) and employ a set of specific values labelled as “fiducial” in Table 1 as a reference for comparison.

The majority of influential model input parameters can be determined, estimated, or constrained using numerical relativity simulations of the BNS merger and early post-merger phase. In particular, \dot{M}_{in} , $v_{\text{ej,in}}$, \bar{B} , $E_{\text{rot,NS,in}}$, P_c , R_e , $M_{\text{NS,in}}$, and $T_{\text{ej,NS,in}}$ can be directly read off from a simulation (e.g., Dessart et al. 2009; Siegel et al. 2014; Siegel & Ciolfi 2015a). Furthermore, the neutrino-cooling timescale t_{ν} can be estimated from the thermal energy content of the NS, given the total neutrino luminosity (e.g., Dessart et al. 2009). The timescale for removal of differential rotation, t_{dr} , can be estimated by the Alfvén timescale, which is given in terms of the magnetic field strength \bar{B} , the radius R_e , and the mass $M_{\text{NS,in}}$ of the NS (Shapiro 2000). In summary, the initial conditions for our model can essentially

be set by an appropriate final snapshot of a BNS merger simulation.

There are further parameters, such as η_{B_p} , I_{pul} , η_{B_p} , η_{TS} , γ_{max} , and Γ_e , which cannot be constrained from simulations of the merger and early post-merger process, as they refer to properties of the pulsar and the PWN in Phase II and III of the evolution. Fortunately, η_{B_p} can largely be absorbed into the parameter \bar{B} (cf. Section 5.1), I_{pul} can essentially be absorbed in $E_{\text{rot,NS,in}}$, varying η_{TS} results in a trivial change (just renormalizing the light curves), and the numerical results are not particularly sensitive to the remaining parameters.

Some of the parameters listed in Table 1 are not varied and, instead, set to some representative value. These are parameters that are either well constrained and do not influence the numerical evolution significantly, only change the results in a trivial way, and/or they can essentially be absorbed into other parameters. One of these parameter values merits further discussion.

The value for η_{TS} corresponds at an order-of-magnitude level to the efficiency of the Crab Nebula in converting pulsar wind power into particle motion, which is currently estimated to be $\gtrsim 10\%$ (Kennel & Coroniti 1984; Bühler & Blandford 2014; Olmi et al. 2015). For PWNe formed in BNS mergers according to our model, this efficiency factor could be different. However, different values for η_{TS} result in different offsets for the light curves, i.e., in a renormalization of the numerical results. Therefore, as long as our model is not used to fit observational data, this parameter can be kept fixed.

Our model characterizes the ejecta material by a mean opacity κ , which we assume to be constant over time, $\kappa = \kappa_{\text{es}} \approx 0.2 \text{ cm}^2 \text{ g}^{-1}$. This value corresponds to Thomson electron scattering, which is the dominant source of opacity at optical and UV wavelengths in the case of iron-rich material (resulting from a high electron fraction). The other important source for opacity of iron-rich material at optical/UV wavelengths, bound-bound absorption, is of the same order of magnitude or less ($\sim 0.1 \text{ cm}^2 \text{ g}^{-1}$; Pinto & Eastman 2000; Kasen et al. 2013). For neutron-rich material (low electron fraction), instead, κ can become as high as $10 \text{ cm}^2 \text{ g}^{-1}$ due to bound-bound opacities generated by transitions of the valence electrons in lanthanide elements (Kasen et al. 2013). However, we assume here that even if the ejecta material was neutron-rich, irradiation from the PWN is strong enough to ensure a very high degree of ionization of the lanthanide elements, such that $\kappa \sim \kappa_{\text{es}}$. At X-ray wavelengths, which is what we are most interested in, an important contribution to the opacity can come from bound-free absorption, depending on the ionization state of the material. Here we assume again that the PWN is sufficiently luminous to ensure a very high degree of ionization of the ejecta material on the timescales of interest, such that $\kappa \sim \kappa_{\text{es}}$. A more detailed computation of the opacity at X-ray wavelengths based on partial ionization of the ejecta material, e.g., along the lines of Metzger et al. (2014) and Metzger & Piro (2014), can, in principle, be included into our model as well. Nevertheless, we take κ as an input parameter of our model (cf. Table 1) and explore the effect of higher values of κ in Section 5.1.

3.2. Assumptions

For the time being, we adopt two further simplifying assumptions. First, we neglect effects of thermal Comptonization in the PWN in Phase III, i.e., we set $\dot{n}_{\text{C}}^{\text{T}} \equiv 0$ in the photon

balance equation (cf. Section 4.3.1 of Paper I). This reduces the procedure of solving the coupled set of integro-differential equations for the photon and particle spectra (Equations (78) and (79) of Paper I) of the PWN to the scheme outlined in Section 5.2 of Paper I, which severely lowers the computational cost for the overall numerical evolution of our model.

Second, for the time being, we neglect effects of further acceleration in Phase III after $t = t_{\text{shock,out}}$, i.e., we set $a_{\text{ej}} \equiv 0$ in Equation (11) of Paper I. This is because we find that for typical input parameter values, the assumption of quasi-stationarity adopted for the description of the radiative processes in the PWN (see Sections 4.3.1 and 5.4 of Paper I) would otherwise not be well satisfied and we expect errors of the order of unity in this case (see also Section 4.2). We therefore postpone a discussion of results for non-zero acceleration of the ejecta shell until a time-dependent framework for the radiative physics of the PWN has been implemented in future work. Such a time-dependent formalism is also required to include a non-zero albedo of the ejecta material, which is why we neglect it here throughout the entire evolution.

4. RESULTS: FIDUCIAL RUN

In this section, we illustrate the numerical evolution of the model equations (Equations (1)–(15) of Paper I) using a typical set of parameter values labelled as “fiducial” in Table 1. This run also serves as a reference for comparison with other parameter settings in the following sections. The results for all other cases are analyzed and interpreted in an analogous way.

4.1. Light Curve

Figure 1 shows the luminosity of escaping radiation from the system throughout the entire evolution. In the following, we discuss the evolution of the system focusing on the top panel, which reports the thermal luminosity L_{rad} (cf. Equations (34), (74), and (100) of Paper I) and non-thermal luminosity $L_{\text{rad,nth}}$ (cf. Equation (104) of Paper I) as computed in the lab frame (rest frame of the NS; cf. Appendix B of Paper I). The evolution of our model can be initialized by data from a numerical relativity simulation (see Section 3.1). We associate the time of merger of the BNS with $t = 0$ and start the numerical evolution of our model a few to tens of milliseconds after merger, typically at $t = t_{\text{min}} = 10^{-2} \text{ s}$, once a roughly axisymmetric state of the NS has been reached.

During Phase I, the NS ejects a significant amount of mass through a baryon-loaded wind (see Section 4.1.1 of Paper I) that carries thermal and EM energy (see Section 4.1.2 of Paper I). Density profiles of this wind for selected times during Phase I are reported in Figure 2. Radiative energy loss from this wind is, however, comparatively inefficient due to the very high optical depth of the ejecta material at these early times (see Figure 3). The total luminosity remains at a level of $\lesssim 10^{39} \text{ erg s}^{-1}$ and rises appreciably only toward the end of Phase I when further mass ejection from the NS is heavily suppressed (see Equation (17) of Paper I) and the bulk of the material has already moved far away from the NS, such that the average density of the baryon-loaded wind and thus the optical depth strongly decreases. This steep decrease of the average density toward the end of Phase I is evident from Figure 2.

At $t = t_{\text{pul,in}}$, once the density in the vicinity of the NS has become sufficiently small, a pulsar magnetosphere is set up and

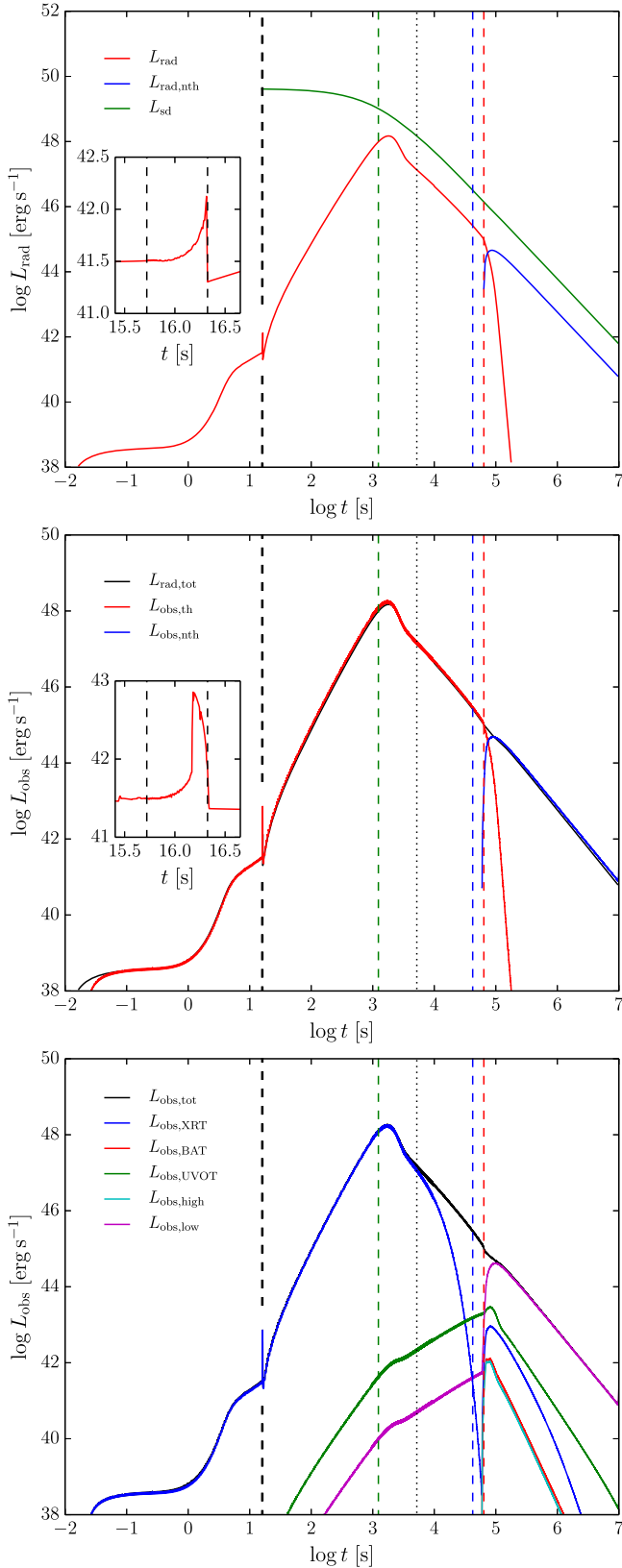


Figure 1. Luminosities throughout Phases I–III for the fiducial parameter setup (cf. Table 1). Phase II is indicated by two black dashed lines (indistinguishable in the logarithmic scale; see also the inset figures), the black dotted line refers to t_{res} . The green, blue, and red dashed lines mark the spin-down timescale and the time of transition to the optically thin regime of the PWN and of the ejecta shell, respectively. Top: lab frame thermal and non-thermal luminosities, together with the spin-down luminosity L_{sd} . Middle: total thermal and non-thermal observer luminosities. Bottom: observer luminosity in different energy bands (cf. Section 2).

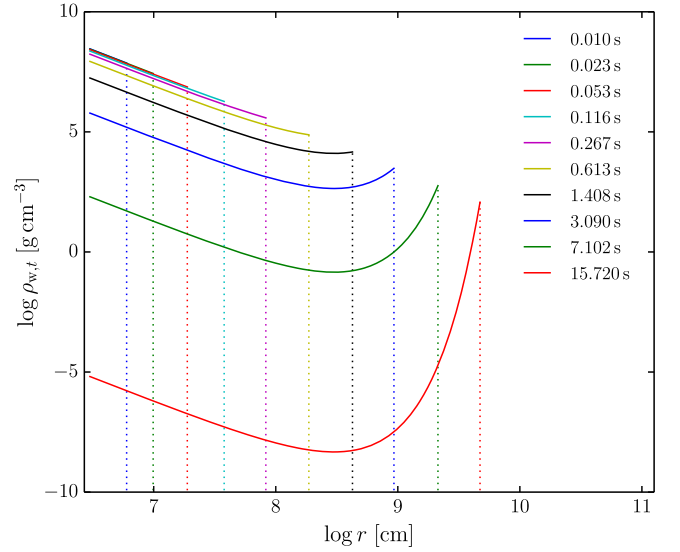


Figure 2. Snapshots of the density profiles of the baryon-loaded wind for selected times during Phase I for the fiducial parameter setup (cf. Table 1). The shape of these profiles is essentially determined by the parameter σ_M (see Table 1 and Section 4.1.1 of Paper I).

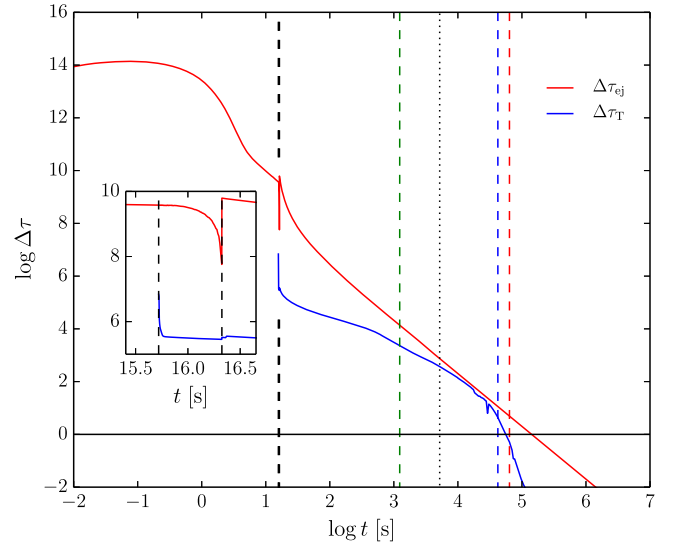


Figure 3. Evolution of the optical depth $\Delta\tau_{\text{ej}}$ of the ejected material (cf. Equations (36), (72), and (103) of Paper I) and of the optical depth $\Delta\tau_T$ of the PWN (cf. Equations (56) and Section 4.3.1 of Paper I) for the fiducial parameter setup (cf. Table 1). Phase II is indicated by two black dashed lines (indistinguishable in the logarithmic scale; see also the inset figure), while the black dotted line refers to t_{res} . The green, blue, and red dashed lines mark the spin-down timescale and the time of transition to the optically thin regime of the PWN and of the ejecta shell, respectively.

Phase II begins (cf. Section 4.2.1 of Paper I). The resulting pulsar wind inflates a PWN behind the less rapidly expanding ejecta. This PWN is highly overpressured with respect to the ejecta material and thus drives a strong shock through it, which sweeps up all the material into a layer of shock-heated ejecta material. Initially, the shock front (denoted by R_{sh} in Figure 4) moves essentially with the speed of light and decelerates to non-relativistic speeds when encountering higher density material shortly before reaching the outer ejecta radius R_{ej} at $t = t_{\text{shock,out}}$ (which terminates Phase II). At any time, this shock front separates the ejecta into shocked ($R_{\text{n}} < r < R_{\text{sh}}$)

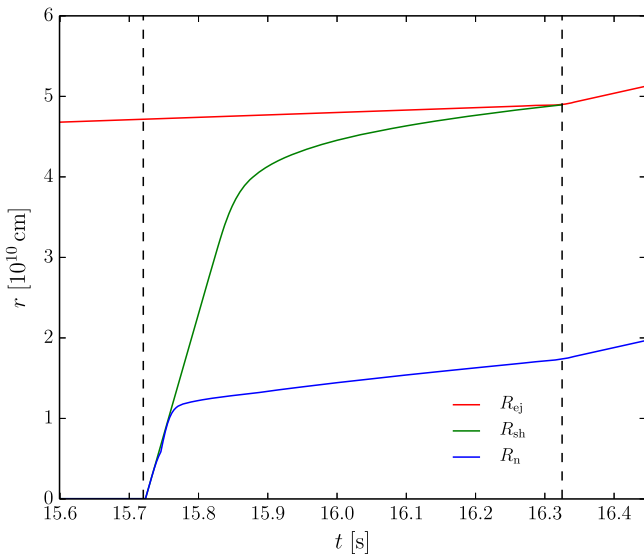


Figure 4. Evolution of three characteristic radii of the system during the shock propagation phase (Phase II) for the fiducial parameter setup (cf. Table 1). The black dashed lines mark the beginning and the end of Phase II. R_{ej} and R_n denote the outer radius of the ejecta material and of the PWN, respectively. The shock front at R_{sh} divides the ejecta layer into shocked and unshocked material.

and unshocked ($R_{sh} < r < R_{ej}$) material, where R_n denotes the outer radius of the PWN. Phase II can be much shorter than Phase I depending on parameters. Its duration is indicated by the black dashed lines in Figures 1, 3, and 4 (see the inset figures, in particular). During this phase the lab-frame luminosity is ever increasing due to a rapidly decreasing optical depth, which, in turn, is caused by the fact that the thickness of the unshocked ejecta layer decreases as the shock front is moving across the baryon-loaded wind.

When $R_{sh} = R_{ej}$ (cf. Figure 4), Phase III begins. A higher expansion speed than in Phase I and II (cf. Section 4.3.2 of Paper I) induces a rapid decrease of the optical depth (cf. Figure 3), which results in a steep rise of the total luminosity. The luminosity reaches its maximum at $\sim 10^{48}$ erg s $^{-1}$ when a significant fraction of the energy reservoir of the ejecta material has been consumed. This maximum brightening of the system occurs at $\sim 10^3$ s, i.e., on the timescale of hours after the BNS merger. We note that this brightening is a very robust feature of our model and it occurs on roughly similar timescales for almost any other set of parameters (see the following sections). If the ejecta shell is further accelerated after $t = t_{shock,out}$ (not considered here for reasons discussed in Section 3.2), this maximum brightening is expected to be shifted to slightly earlier times. Preliminary results indicate that in determining this timescale, acceleration is likely to dominate other effects such as employing different opacities.

After having radiated away most of its energy, the ejecta shell enters an asymptotic regime, in which the internal energy of the ejecta layer is essentially determined by the flux of inflowing energy from the PWN. The energy deposited and thermalized in the ejecta shell per time step is again radiated away during the same time step, thanks to the ever decreasing photon diffusion timescale of the ejecta shell. Hence, there is no further energy acquisition anymore. In this regime, the overall luminosity is determined by the luminosity of escaping

photons from the PWN, which is again set by the spin-down luminosity L_{sd} of the pulsar as the PWN conserves energy (see Appendix D of Paper I and the discussion in Section 5.6 of Paper I). Therefore, the total luminosity follows the spin-down luminosity (green line in the top panel of Figure 1; see also Section 4.2.1 of Paper I) at a constant ratio set by the efficiency factor η_{TS} (cf. Table 1). Hence, it also shows the characteristic $\propto t^{-2}$ scaling at late times $t \gg t_{sd}$, where t_{sd} is the spin-down timescale (cf. Section 4.2.1 of Paper I; indicated by the green dashed line in Figures 1 and 3).

In this asymptotic regime, the evolution equation for E_{th} (Equation (14) of Paper I) becomes stiff and an alternative scheme is used to further evolve the set of coupled differential equations of our model (see the discussion in Section 5.6 of Paper I). The transition time at which we switch over to this alternative formulation is called t_{res} , and it is indicated by a black dotted line in Figures 1 and 3.

As the optical depth approaches unity the ejecta shell becomes transparent to the radiation from the PWN. From Equations (99) and (103) of Paper I, one obtains the scaling $\Delta\tau_{ej} \propto R_{ej}^{-2} \propto t^{-2}$, where the second proportionality assumes a constant expansion speed. This scaling only holds once the shell thickness Δ_{ej} has become much smaller than R_{ej} , which is not yet the case at $t = t_{shock,out}$ for the fiducial run as illustrated by Figure 4. From Figure 3 it is evident, however, that this scaling is reached at times $t \gtrsim 10^2$ s. Once $\Delta\tau_{ej}$ has approached unity, radiation from the PWN is not absorbed anymore by the ejecta material, such that the thermal emission from the ejecta surface rapidly decreases and, instead, non-thermal radiation from the PWN is emitted toward the observer (cf. Figure 1). This transition from predominantly thermal to non-thermal spectra is discussed in more detail in Section 4.3. The time of transition between the optically thick and thin regime is indicated by a red dashed line in Figures 1 and 3. We refer to Section 4.3.3 of Paper I for a discussion of how this transition is implemented in the model evolution equations.

As the PWN conserves energy (see Appendix D of Paper I), the total non-thermal luminosity $L_{rad,nth}$ also scales as L_{sd} once the ejecta shell is optically thin. We note that in the fiducial setup, the PWN becomes optically thin prior to the ejecta matter (see Figure 3). Hence, radiation from the deep interior of the nebula is already being emitted toward the observer once the PWN radiation is free to escape from the system.

The middle panel of Figure 1 shows the total thermal and non-thermal luminosity ($L_{obs,th}$ and $L_{obs,nth}$) as seen by a distant observer in comparison with the total lab-frame luminosity L_{rad} . These observer light curves are reconstructed using the method presented in Section 5.7 of Paper I and take into account the combined effects of relativistic beaming, the relativistic Doppler effect, and the time-of-flight effect for radiation emerging from the surface and/or the interior of a relativistically expanding sphere. As the expansion speed of the ejecta material ($v_{ej,in} = 0.01c$ in Phase I and II, $v_{ej} = 0.064c$ in Phase III; cf. Section 4.3.2 of Paper I) remains non-relativistic for the fiducial setup (as we are neglecting further acceleration for the time being, see Section 3.2), these relativistic effects induce only small corrections to the observer light curve, which closely follows the lab-frame light curve.

The delayed onset of the observer luminosity with respect to L_{rad} at very early times is due to the time-of-flight effect: radiation from high latitudes (small θ) of the expanding sphere

reaches the observer earlier than radiation from lower latitudes (high θ , where $\theta = 0$ defines the direction of the observer; see Section 5.7 of Paper I for more details). The offset between the time grids of the lab frame and the remote observer is calibrated in such a way that a photon emitted from the spherical surface of the expanding ejecta at $\theta = 0$, $r = R_{\min}$, with R_{\min} being the inner spatial boundary of our model, at a time $t = t_{\min}$ after the BNS merger is received by the observer at a time $t' = t_{\min}$ (see Section 5.7 of Paper I). This time-of-flight effect is also evident during Phase II, where the peak observer luminosity appears to precede the end of Phase II by $R_{\text{ej}}(t_{\text{shock,out}})/c \approx 0.16$ s (compare the inset figures in the two upper panels of Figure 1). This is because the main contribution to the observer luminosity originates from high latitudes, while the delayed radiation from low latitudes only forms a tail that broadens the peak. Furthermore, we note that the thermal observer luminosity is slightly higher than the lab-frame luminosity in Phase III, which is due to the relativistic Doppler effect. Finally, the time-of-flight effect can be noticed again when the ejecta shell becomes optically thin. The onset of the non-thermal radiation as seen by the observer precedes the corresponding onset in the lab frame (red-dashed line in Figure 1) by R_n/c . Moreover, the observer light curve starts to deviate from the lab-frame light curve at very late times (barely visible in Figure 1). This is because the PWN is optically thin and radiation from the entire volume of the nebula can reach the observer. As radiation is being delayed while the overall luminosity is decreasing, this results in a less steep slope for the observer light curve.

In summary, the relativistic corrections to the light curve are very small and barely visible for the fiducial parameter setup. However, for higher velocities and/or in presence of further acceleration during Phase III, these relativistic corrections can significantly reshape the observer light curve, which needs to be taken into account when comparing the predictions of our model to observational data.

The total energy radiated away from the system is distributed over many orders of magnitude in frequency. Depending on the energy band of interest, very different morphologies for the observer light curves are obtained (cf. the lower panel of Figure 1). A remarkable feature evident from Figure 1 is that the typical temperature of the ejecta shell during Phase I, II, and up to the time of maximum brightening in Phase III corresponds to an energy in the X-ray band, such that almost all of the radiated energy falls into the sensitivity regime of the XRT instrument. This is a very robust feature that we also find in case of almost all other parameter settings: the radiation from the system up to its maximal brightness is predominantly thermal and of X-ray nature. Soon after this, the UV and optical emission dominates, until, finally, most of the energy is radiated away in the radio band once the ejecta shell becomes transparent to the radiation from the nebula. This radio emission is generated by synchrotron cooling of the electron-positron pairs in the PWN (see also Section 4.3). Nevertheless, appreciable X-ray luminosities of the order of $\sim 10^{42}$ erg s $^{-1}$ may still be present at times as late as $t \sim 10^5$ s. For the remainder of this paper, we focus specifically on X-ray luminosities and spectra, as they appear to be most relevant in the context of early afterglows of a BNS merger event.

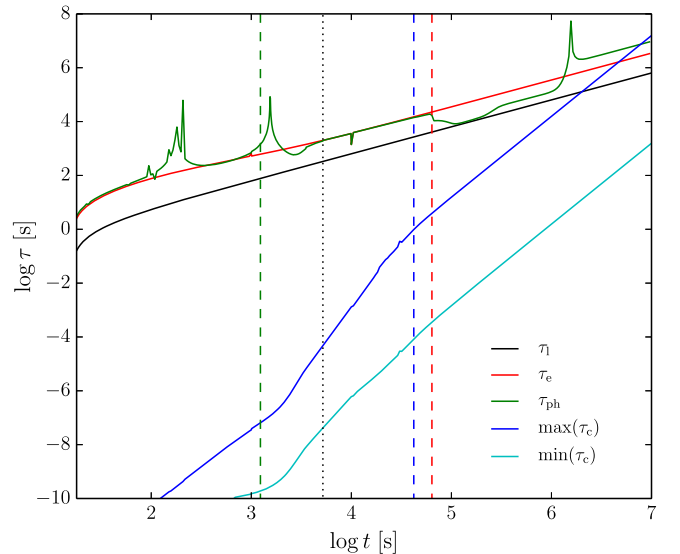


Figure 5. Evolution of several characteristic timescales related to the radiative processes in the PWN throughout Phase III for the fiducial parameter setup (cf. Table 1). Shown are the light crossing time τ_1 of the nebula, the timescales for change of particle and photon injection, τ_e and τ_{ph} , respectively, and the minimum and maximum value over frequency for the total particle cooling timescale τ_c in the nebula. The green, blue, and red dashed lines indicate the spin-down timescale and the time of transition to the optically thin regime of the PWN and of the ejecta shell, respectively. The black dotted line corresponds to $t = t_{\text{res}}$ (see Section 4.1).

4.2. Monitoring the Constraints

Our approach for modeling the radiative processes in the PWN (cf. Section 4.3.1 of Paper I) is based upon two important assumptions: quasi-stationarity and negligible influence of synchrotron self-absorption. The validity of these assumption needs to be routinely verified during the numerical integration of the model evolution equations. As discussed in Sections 5.4 and 5.5 of Paper I, this can be achieved by monitoring several timescales and the optical depth to synchrotron self-absorption, which we shall discuss here.

Figure 5 reports the evolution of the light crossing time τ_1 of the nebula, the timescales for change of particle and photon injection into the nebula (τ_e and τ_{ph} , respectively), and the total particle cooling timescale τ_c of the nebula throughout Phase III (for definitions, see Section 5.4 of Paper I). In general we find that

$$\tau_c \ll \tau_{\text{ph}}, \tau_c \ll \tau_e, \quad (2)$$

which shows that the nebula particle distribution can adjust fast enough to changes of the exterior conditions and thus justifies the assumption of stationarity concerning the particle distribution in the nebula (see Section 5.4 of Paper I). Only at late times $t \gtrsim 10^7$ s these conditions are not satisfied anymore for part of the particle energy spectrum. However, we are not interested in the evolution of the system at such late times. This is a general result that qualitatively holds throughout the parameter space considered in Table 1: at times of interest, the stationarity assumption regarding the particle distribution is very well satisfied. Moreover, Figure 5 also shows that typically

$$\tau_1 \ll \tau_{\text{ph}}, \quad (3)$$

except for a short transition phase around $t \sim 10^5$ s. This is the time when the ejecta shell becomes optically thin and the

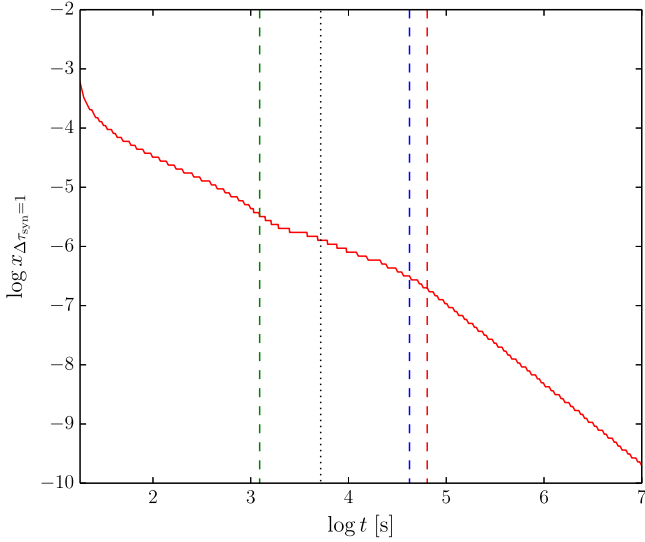


Figure 6. Evolution of the normalized dimensionless photon frequency $x_{\Delta\tau_{\text{syn}}=1}$ (cf. Section 5.5 of Paper I) in Phase III for the fiducial parameter setup (cf. Table 1). This frequency separates the optically thick ($x < x_{\Delta\tau_{\text{syn}}=1}$) from the optically thin ($x > x_{\Delta\tau_{\text{syn}}=1}$) parts of the spectrum of the PWN to synchrotron self-absorption. The X-ray band is always optically thin to this process. The green, blue, and red dashed lines indicate the spin-down timescale and the time of transition to the optically thin regime of the PWN and of the ejecta shell, respectively. The black dotted line corresponds to $t = t_{\text{res}}$ (see Section 4.1).

timescale for change of the photon spectrum is mostly determined by the auxiliary function f_{ej} to model this transition (cf. Section 4.3.3 of Paper I). In general and across the parameter space we find, however, that Equation (3) is well satisfied, which justifies the stationarity assumption concerning the photon distribution inside the PWN (see Section 5.4 of Paper I). This picture can change when further acceleration of the ejecta shell during Phase III is considered. We find that in this case τ_{ph} can become similar to τ_1 and errors of the order of unity for the photon and particle spectra are expected. This is why we refrain from discussing results for this case in the present paper. To overcome this problem, a time-dependent framework for the radiative processes in the nebula has to be developed, which we postpone to future work.

Figure 6 monitors the validity of the second central assumption: negligible influence of synchrotron self-absorption. It shows the normalized dimensionless frequency which separates the optically thick and thin regimes of the photon spectrum to synchrotron self-absorption (for a definition, see Section 5.5 of Paper I). As we have $x_{\Delta\tau_{\text{syn}}=1} < 4 \times 10^{-4}$ except for the first few time steps in Phase III, the spectrum in the XRT band (which is what we are mostly interested in) is unlikely to be affected by effects of synchrotron self-absorption. We find that this conclusion typically also holds across the entire parameter space considered in Table 1.

4.3. Spectra

After having discussed the light curves for the fiducial parameter setup in Section 4.1, this subsection presents results for the associated spectral evolution.

Figure 7 shows the intrinsic spectrum $L_{\text{PWN}}(\nu, t)$ of the radiation escaping from the nebula for selected times during

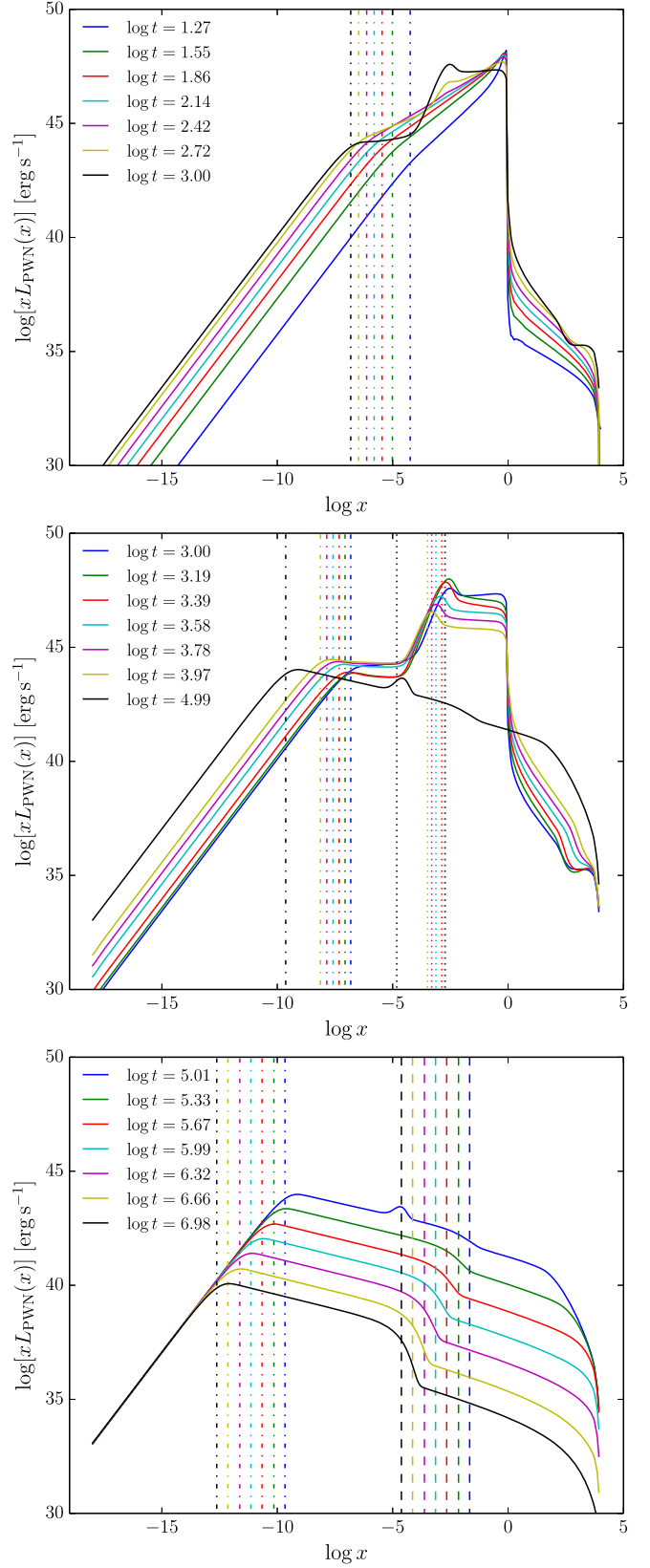


Figure 7. Luminosity of escaping radiation from the nebula as a function of $x = h\nu/m_e c^2$ for selected times during Phase III (fiducial parameters, cf. Table 1). Dot-dashed and dashed lines refer to the critical frequencies $\nu_{c,\gamma_{\text{min}}}$ and $\nu_{c,\gamma_{\text{max}}}$, respectively (see the text). Dotted lines indicate the frequency at maximum of the thermal input spectra.

Phase III (cf. Equation (91) of Paper I). These spectra result from the numerical solution to the photon and particle balance equations in the PWN (cf. Section 4.3.1 of Paper I) and account for the combined effects of synchrotron losses, (inverse) Compton scattering, pair production and annihilation, Thomson scattering off thermal particles, and photon escape.

At low frequencies, the spectra are dominated by synchrotron radiation. The spectrum peaks at a frequency around $\nu_{c,\gamma_{\min}}$ (cf. the dot-dashed lines in the three panels), where

$$\nu_{c,\gamma} = \frac{3}{4\pi} \frac{eB_n}{m_e c^2} \gamma^2 \quad (4)$$

is the critical frequency above which the synchrotron spectrum of a single radiating particle of Lorentz factor γ sharply decreases, and $\gamma_{\min} = 1$ is the minimum Lorentz factor of the particle distribution (see also Appendix C of Paper I). The synchrotron spectrum extends up to $\nu_{c,\gamma_{\max}}$ (cf., e.g., the dashed vertical lines in the bottom panel) and shows power-law decline between $\nu_{c,\gamma_{\min}}$ and $\nu_{c,\gamma_{\max}}$. In particular, this is evident at late times (bottom panel), when the spectrum is dominated by synchrotron radiation below $\nu_{c,\gamma_{\max}}$. This behavior reflects the underlying particle distribution $N(\gamma)$ (cf. Section 4.3.1 of Paper I), which is also of power-law nature at late times.

At UV and higher energies other processes can determine the spectral shape. One prominent feature is typically caused by the strong photon field with luminosity $L_{\text{rad, in}}$ of thermal radiation from the inner surface of the confining ejecta envelope (cf. Equation (101) of Paper I). A corresponding thermal ‘‘bump’’ becomes visible around $\log t \approx 2.7$ (cf. the upper panel) and persists until the ejecta material becomes optically thin around $\log t \approx 5$. The maxima of the thermal injection spectra at energies corresponding to $\approx 2.8 k_B T_{\text{eff}}$ are indicated by dotted lines in the middle panel, where $T_{\text{eff}}^4 = T_{\text{eff, com}}^4 / \zeta \gamma_{\text{ej}}$ defines the effective temperature of the ejecta material as measured in the lab frame (see Equation (101) of Paper I). It is the full non-linear interaction of these injected photons with the particle distribution via (inverse) Compton scattering and pair creation/annihilation that essentially determines the spectral shape from UV to gamma-ray energies up to $x_{\max} = \gamma_{\max}$.

The non-thermal radiation escaping from the PWN is reabsorbed and thermalized by the surrounding ejecta layer as long as the confining envelope is optically thick. The spectra as seen by a remote observer are thus characterized by thermal spectra at early times (cf. Figure 8, upper panel), a transition from thermal to non-thermal spectra when the ejecta material becomes optically thin (cf. Figure 8, middle panel), and non-thermal spectra at late times (cf. Figure 8, bottom panel). We refer to Section 5.7 of Paper I for a discussion of how these observer spectra are reconstructed. The thermal part of the spectrum is plotted as dotted curves in the lower two panels and shows how quickly this contribution fades away when the optical depth of the ejecta approaches unity. We note that the effective temperature of the ejecta material at early times falls into the XRT band, which typically also holds for all other runs across the entire parameter space (see also Section 4.1). This is a remarkable feature that makes XRT an ideal instrument to observe and analyze the radiation escaping from the system at $\lesssim 10^4$ – 10^5 s after the BNS merger.

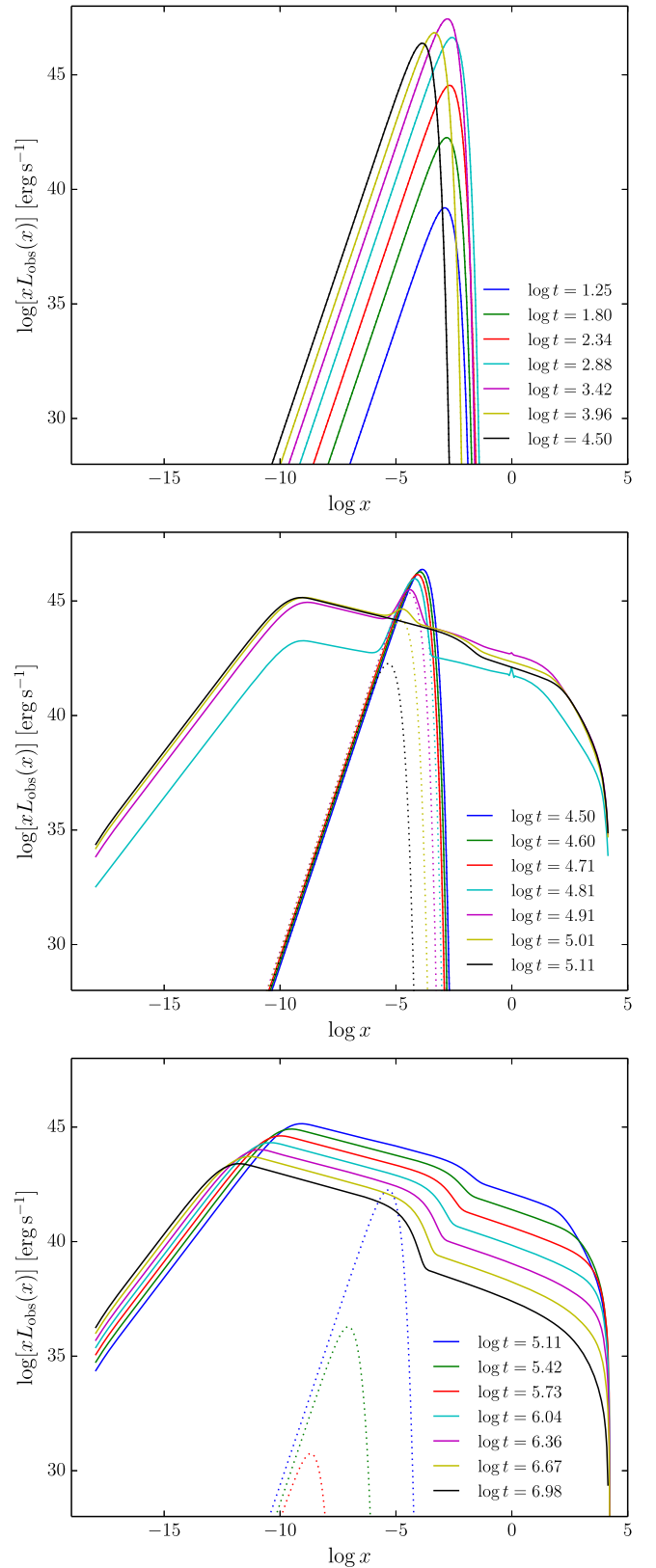


Figure 8. Luminosity of escaping radiation from the system as seen by a remote observer (cf. Section 2) as a function of $x = h\nu/m_e c^2$ for selected times during Phase III and the fiducial parameter setup (cf. Table 1). Dotted curves indicate the thermal contribution separately. The middle panel shows the transition from thermal to non-thermal emission.

According to our model, the observable radiation at early times is purely thermal. However, due to the high degree of ionization of the material, there are numerous free electrons upon which photons can inverse Compton-scatter to form a non-thermal high-energy tail of the spectrum. Furthermore, we have employed a single effective temperature to characterize the ejecta layer. The ejecta shell will, however, be characterized by strong temperature gradients, which will give rise to a superposition of individual Planck spectra of different temperatures. Hence, the actual observable spectrum at early times might be different from the simple Planck spectrum employed here and could even appear as a power law in the XRT band. The transition from this “thermal” spectrum at early times to an intrinsically non-thermal spectrum at later times, which carries the signatures of the PWN, is a characteristic prediction of our model that is common to essentially all parameter settings. The timescale for this transition depends on the optical thickness of the ejecta material, which depends on a number of parameters, such as the initial density of the ejecta shell (i.e., t_{dr} , \dot{M}_{in} , σ_M), its opacity κ , and the expansion velocity v_{ej} . Depending on these parameters, it can occur significantly earlier than for the fiducial parameter set.

5. RESULTS: INFLUENCE OF PARAMETERS

Most of the energy radiated away from the system at timescales of interest is contained in the X-ray band (cf. the previous section). This section is devoted to study the influence of individual model input parameters (see Table 1) on the numerical result for the X-ray light curves as seen by a remote observer. We discuss and compare results for the XRT band varying only one parameter at a time. We distinguish between “non-collapsing” models, for which we arbitrarily set $f_{\text{coll}} = \infty$, and “collapsing” models, in which the NS collapses to a black hole at a fraction or multiple of the spin-down timescale (set by f_{coll} , see Table 1).

5.1. Non-collapsing Models

Non-collapsing model runs correspond to a scenario in which the merger results in an NS that is indefinitely stable against gravitational collapse. We restrict the discussion here to those parameters that influence the model results significantly, i.e., \bar{B} , η_{B_p} , t_{dr} , \dot{M}_{in} , $E_{\text{rot,NS,in}}$, and κ . We find that the predictions of our model concerning the dynamics of the system and the observer light curves are not significantly influenced by the remaining parameters.

Figure 9 compares the prediction for the X-ray light curve in the XRT band and the fiducial parameter setup (cf. Table 1) with runs employing different values for \bar{B} , η_{B_p} , t_{dr} , and \dot{M}_{in} . The top panel shows that a higher total initial magnetic field strength in the outer layers of the newly formed NS already leads to an appreciably higher X-ray luminosity in Phase I and II. This is because the baryon-loaded wind is endowed with a much higher Poynting flux for higher values of \bar{B} , which is dissipated in the ejecta material ($L_{\text{EM}} \propto \bar{B}^2$; cf. Equation (32) of Paper I). At the beginning of Phase III, higher values of \bar{B} lead to a significantly steeper rise of the luminosity, because the dipolar magnetic field strength at the pole of the NS, B_p , is also higher (cf. Equation (41) of Paper I). As the spin-down luminosity scales as $L_{\text{sd}} \propto B_p^2$ (cf. Section 4.2.1 of Paper I) and

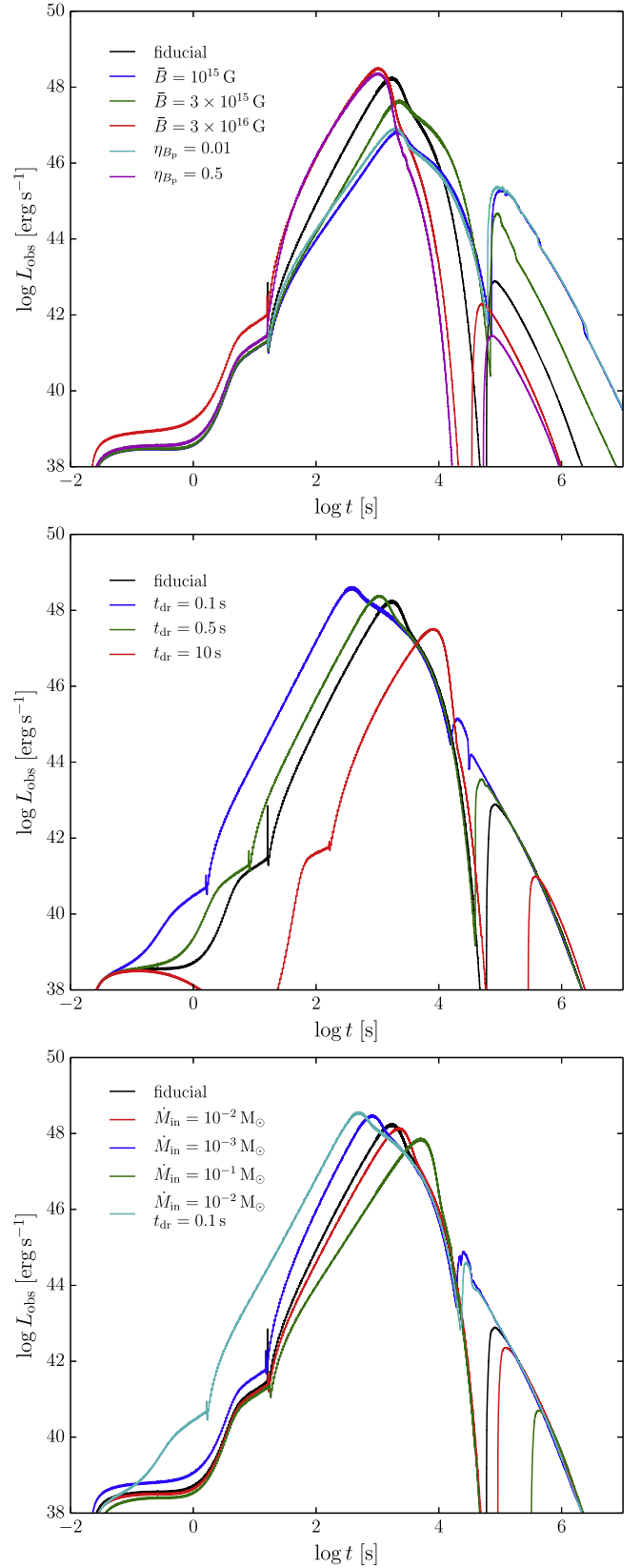


Figure 9. Luminosity $L_{\text{obs,XRT}}$ of radiation in the XRT band as seen by a remote observer (cf. Section 2) for the fiducial parameter setup (cf. Table 1) and different values of \bar{B} and η_{B_p} (top), different values of t_{dr} (middle) and different values of \dot{M}_{in} (bottom). Phase II of the evolution is comparatively short and can be noticed by the kink in the light curves between 1 and 10^2 s.

the PWN conserves energy (cf. Appendix D of Paper I), more energy is deposited in the ejecta material at earlier times. Furthermore, the maximum value for the luminosity is essentially determined by L_{sd} ⁵ which is why the maxima of the runs spread over two orders of magnitude. The time of this maximal brightening of the system is roughly $\sim 10^3$ s and varies only marginally among the different runs. This timescale is essentially determined by the optical depth of the ejecta shell, which does not directly depend on \bar{B} (see also below). After the maximum in the luminosity, the light curve decays steeper for higher values of \bar{B} , which is due to the fact that the spin-down timescale scales as $t_{\text{sd}} \propto B_p^{-2}$ and, hence, energy injection into the ejecta material fades away more rapidly. Moreover, it is important to note that varying either \bar{B} or η_{B_p} by the same factor yields roughly identical results in Phase III (compare the cyan and blue and the red and purple lines, respectively). This is because with all other parameters being identical, those runs also share the same value of B_p , which determines the spin-down luminosity and therefore the energy output in Phase III. In Phase I, however, the luminosity differs, as \bar{B} directly enters the source term L_{EM} (see above). Consequently, as far as Phase III is concerned, the parameter η_{B_p} can be absorbed into \bar{B} .

The parameter t_{dr} is highly influential in determining timescales, as shown by the middle panel of Figure 9. With all other parameters fixed, it does not only set the duration of Phase I, which is directly proportional to t_{dr} (the timescale for the density in the surrounding of the NS to decrease is t_{dr}/σ_p ; see Sections 4.1.1 and 4.2.1 of Paper I). It also impacts the time of maximum brightness, which lies between $\sim 10^2$ – 10^4 s for the cases considered here. This is because with higher values of t_{dr} , the total ejected mass $M_{\text{ej}} \approx \dot{M}_{\text{in}} t_{\text{dr}}/\sigma_M$ (cf. Equation (31) of Paper I) increases and thus the ejecta shell needs more time to expand in order to reach a comparable average density and thus a comparable optical depth. At the same time, however, the material cools down, which leads to a lower peak brightness as t_{dr} increases.

Smaller initial mass loss rates \dot{M}_{in} induce moderately higher luminosities in Phase I, II, and up to the global maximum of the X-ray light curve in Phase III (see bottom panel of Figure 9), thereby also shifting the time of maximum brightness to earlier times. This is because lower values of \dot{M}_{in} result in a smaller amount of ejected mass $M_{\text{ej}}(t)$ up to time t in Phase I (cf. Equation (31) of Paper I) and, hence, in a lower average density and optical depth of the ejecta material. As the total amount of ejected material $M_{\text{ej}} \approx \dot{M}_{\text{in}} t_{\text{dr}}/\sigma_M$ is also reduced, the ejecta shell starts off with a lower average density at $t = t_{\text{shock,out}}$ and is thus characterized by a lower optical depth throughout Phase III. The red line in the lower panel of Figure 9 corresponds to a case in which both t_{dr} and \dot{M}_{in} differ from the fiducial value, but combine to give the same total ejected mass as in the $\dot{M}_{\text{in}} = 10^{-3} M_{\odot}$ case (blue curve). The evolution up to the global maximum is different in the two cases, showing that the two parameters cannot be reduced to a single one (e.g., to M_{ej}). This is because t_{dr} has a much stronger effect on shifting the onset of Phase II. However, on much longer timescales this shift becomes irrelevant and the two curves essentially agree.

Different initial rotational energies of the newly born NS after merger affect the X-ray light curve only by rescaling the global maximum (see the top panel of Figure 10). This scaling

⁵ A rough estimate for the maximum possible X-ray observer luminosity in absence of strong relativistic effects is given by $\sim \eta_{\text{TS}} L_{\text{sd,in}}$, were $L_{\text{sd,in}}$ is the initial spin-down luminosity at $t = t_{\text{put,in}}$ (cf. Section 4.2.1 of Paper I).

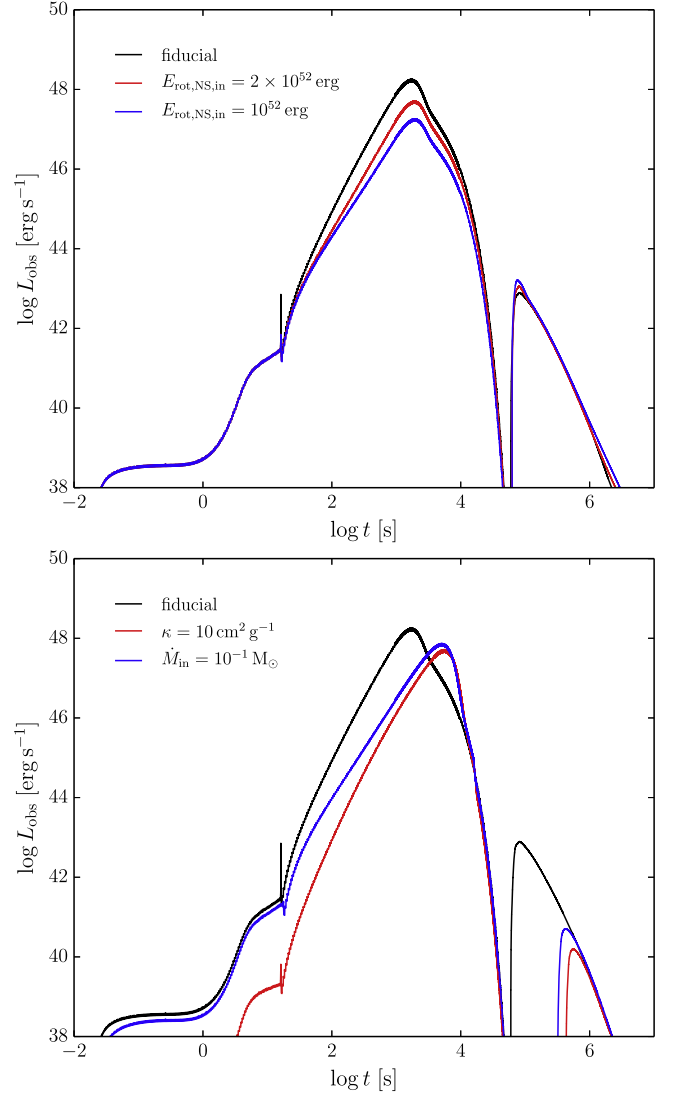


Figure 10. Luminosity $L_{\text{obs,XRT}}$ of radiation in the XRT band as seen by a remote observer (cf. Section 2) for the fiducial parameter setup (cf. Table 1) and different values of $E_{\text{rot,NS,in}}$ (top) and different values of the opacity κ (bottom). Phase II of the evolution is comparatively short and can be noticed by the kink in the light curves between 1 and 10^2 s.

can roughly be explained by the fact that $L_{\text{sd,in}} \propto E_{\text{rot,NS,in}}^2$ (assuming that the rotational energy of the pulsar is approximately given by $E_{\text{rot,NS,in}}$; cf. Section 4.2.1 of Paper I). This is similar to the scaling found for \bar{B} and η_{B_p} (see above).

Figure 10 (bottom panel) shows the effect of a much higher (by a factor of 50) mean opacity κ than in the fiducial case (cf. the discussion in Section 3.1). This increases the optical depth, which thus results in a dimmer X-ray light curve and a delayed global maximum (as it takes more time to radiate away the acquired energy). The cooling timescale of the ejecta material after the global maximum in the luminosity, however, depends mostly on the energy input, which is similar in the two runs. Therefore, both light curves fall off in a very similar way after $\sim 10^4$ s as the temperature of the Planck spectrum moves out of the XRT band. Furthermore, we note that concerning the behavior in Phase III, higher opacities have a very similar effect as a higher initial mass-loss rate for the baryonic wind in Phase I, as shown by the blue curve. This shows that part of the

uncertainty in the opacities can effectively be absorbed into, e.g., the initial mass-loss rate.

5.2. Collapsing Models

Collapsing models correspond to the most frequent case in which the NS is supramassive (or hypermassive) at birth (cf. Section 1 of Paper I) and it is thus doomed to collapse to a BH. Everything that has been noted in Section 4 and in the previous subsection still applies (at least up to the time of collapse), with the additional complication that the NS collapses to a BH at $t = t_{\text{coll}}$, which alters the subsequent evolution of the system. After $t = t_{\text{coll}}$, the evolution equations are numerically integrated as described in Section 4.4 of Paper I. We first concentrate on the more likely case of a gravitational collapse during Phase III (Section 5.2.1), and return to the possibility of a collapse during Phase I in Section 5.2.2.

5.2.1. Collapse During Phase III

If the NS is supramassive at birth it can survive until a substantial fraction of its rotational energy has been dissipated. Its lifetime is therefore expected to be of the order of the spin-down timescale t_{sd} . The top panel of Figure 11 shows the evolution of the system for the fiducial parameter set, but different times of collapse. Dotted lines indicate $t = t_{\text{coll}}$, which is set in units of t_{sd} by the parameter f_{coll} (see Table 1).

If the collapse occurs prior to the time of maximal brightening, it manifests itself only as a ‘‘kink’’ in the X-ray light curve (cf., e.g., the blue curve). The latter still increases up to a maximum after the time of collapse due to the fact that there is still a substantial amount of internal energy (stored in the ejecta material) yet to be radiated away. The sooner the time of collapse, the dimmer is this global maximum of the light curve, since further energy injection by L_{PWN} is substantially reduced at $t = t_{\text{coll}}$ (see below). After the maximum the light curve gradually decreases (cf. blue and green curves) until a plateau-like phase is reached.

In contrast, if the NS collapses after the time of maximal brightening, the light curve directly decreases to a plateau-like phase. This is because the ejecta shell enters an ‘‘asymptotic’’ phase shortly after having reached the global maximum (cf. Section 5.6 of Paper I). In this phase, most of the acquired internal energy has already been radiated away and the present luminosity depends on the present influx of energy from the PWN. This influx is severely reduced after $t = t_{\text{coll}}$, as only gradual cooling of the PWN can still supply the ejecta shell with further energy (as described in Section 4.4 of Paper I).

It is this supply with residual energy from the PWN that creates the plateau phase characteristic of all runs across the entire range for f_{coll} (cf. the upper panel of Figure 11). The characteristics of the light curves after $t = t_{\text{coll}}$ are, however, better illustrated by plotting the luminosity as a function of the time after collapse (cf. the bottom panel of Figures 11 and 12).

Depending on the collapse time, the light curves show a characteristic two-plateau structure after $t = t_{\text{coll}}$ (cf. the bottom panel of Figures 11 and 12). Only for early collapse times, the light curve essentially shows a single rising plateau plus a ‘‘bump’’ of radiation (cf., e.g., the case $f_{\text{coll}} = 0.1$) caused by the release of energy stored in the ejecta shell (see above). In this case, the light curve after $t = t_{\text{coll}}$ strongly depends on the previous history as the radiation escaping from the system is still sourced by energy acquired by the ejecta material prior to

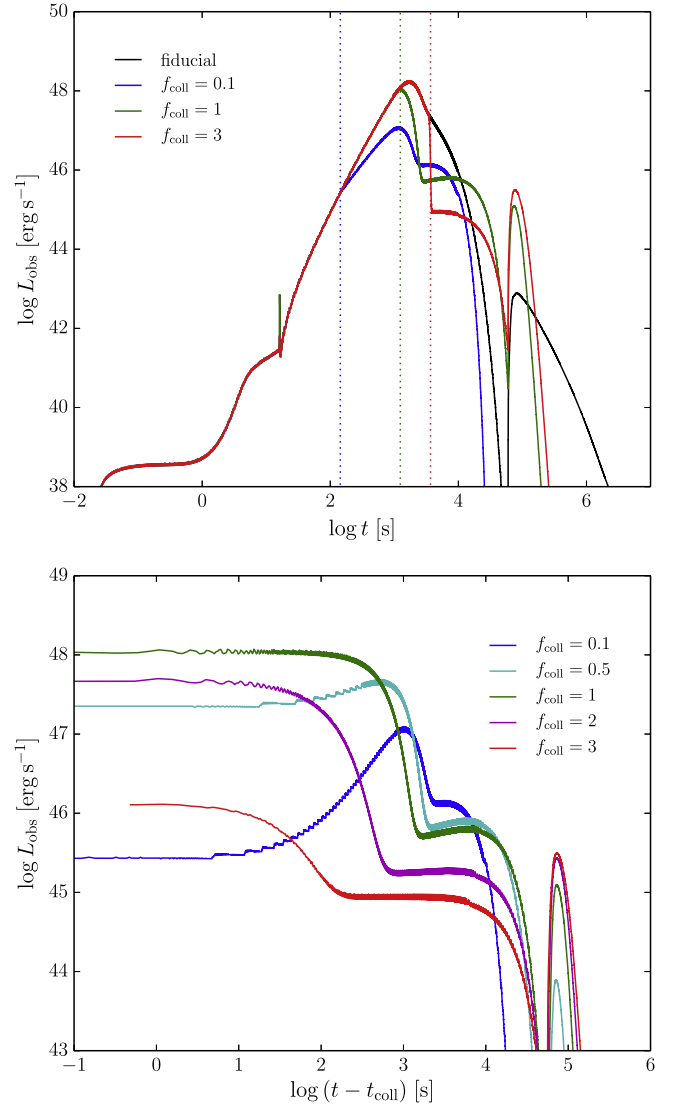


Figure 11. Top: luminosity $L_{\text{obs,XRT}}$ of radiation escaping from the system in the XRT band as seen by a remote observer (cf. Section 2) for the fiducial parameter setup (cf. Table 1) and different values of f_{coll} . Dotted lines indicate the time of collapse t_{coll} of the NS in the lab frame. Bottom: same light curves as in the top panel (plus additional ones), but as a function of the time after the respective collapse. The latter light curves represent the ‘‘X-ray afterglow’’ in the time-reversal scenario.

the collapse. However, for runs in which the ejecta shell has already entered or is about to enter the asymptotic regime (see above; cf., e.g., the cases $f_{\text{coll}} = 1, 2, 3$) its properties strongly depend on the present state of the nebula and the total observer luminosity $L_{\text{obs,tot}}$ clearly shows a two-plateau structure (see the bottom panel of Figure 12). The duration of the first plateau in these runs can be roughly estimated by the photon diffusion timescale $t_{\text{diff,ej}}$ of the ejecta layer at the time of collapse (cf. Equation (122) of Paper I and the top panel of Figure 12). This timescale represents the time needed for the ejecta material to adjust to the sudden (instantaneous) change of the PWN conditions at $t = t_{\text{coll}}$.⁶ The latter process is nicely reflected by

⁶ We note that the collapse of the NS proceeds on the dynamical timescale, which is of the order of milliseconds. At the times of interest here, the collapse can thus be implemented as an instantaneous modification of the numerical integration of the evolution equations at $t = t_{\text{coll}}$ (see also Section 4.4 of Paper I).

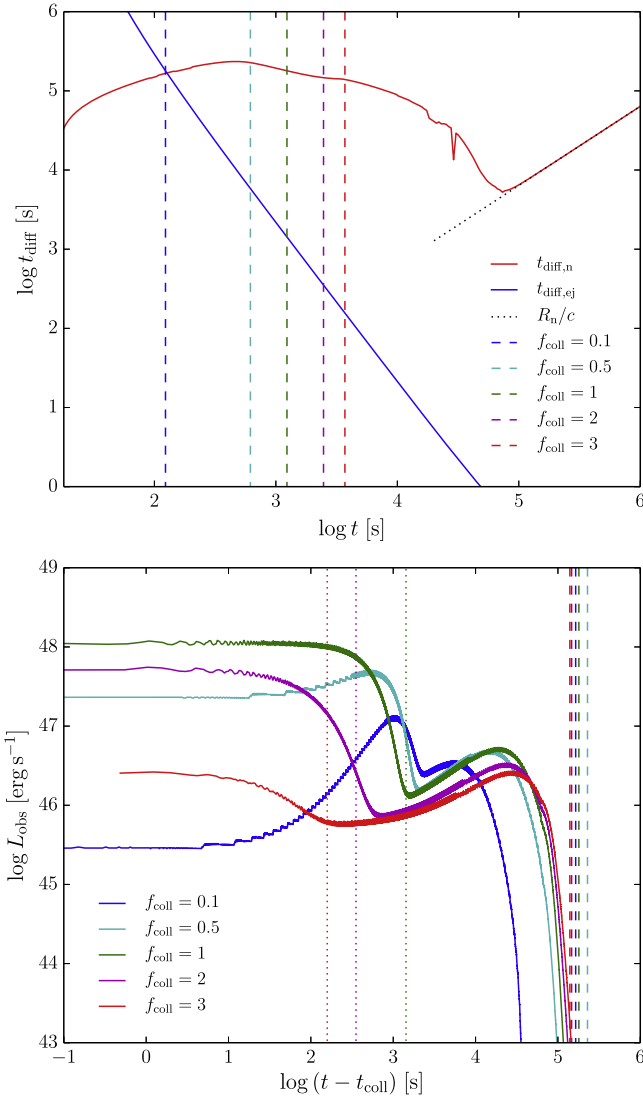


Figure 12. Top: photon diffusion time of the PWN ($t_{\text{diff,n}}$) and of the ejecta shell ($t_{\text{diff,ej}}$) for the fiducial parameter setup (cf. Table 1) and $f_{\text{coll}} = \infty$, i.e., without a collapse of the NS to a black hole. Dashed lines indicate the different times of collapse considered in Figure 11. Bottom: total luminosity $L_{\text{obs,tot}}$ (cf. Section 2) as seen by a remote observer after the respective collapse, corresponding to the runs depicted in the bottom panel of Figure 11. Dashed lines represent $t_{\text{diff,n}}$ at the time of collapse (cf. the upper panel), which represent upper limits on the duration of the second “plateau” evident in these light curves. Dotted lines indicate $t_{\text{diff,ej}}$ at the time of collapse for the runs with $f_{\text{coll}} \geq 1$, which provide an estimate for the duration of the first plateau for these runs.

the aforementioned light curves depicted in the lower panel of Figure 12, in which case $t_{\text{diff,ej}}$ at the time of collapse (indicated by dotted lines) indeed provides reliable predictions for the duration of the first plateau.

The duration of the second plateau phase in the total observer luminosity $L_{\text{obs,tot}}$ (cf. Section 2) is essentially determined by the photon diffusion time $t_{\text{diff,n}}$ of the PWN (cf. Section 4.4 of Paper I and the top panel of Figure 12), which sets the cooling timescale of the nebula after the collapse. As $t_{\text{diff,n}}$ is monotonically decreasing after $t = t_{\text{coll}}$ (cf. Equation (105) and (106) of Paper I), the diffusion time at $t = t_{\text{coll}}$ provides an upper bound on the plateau duration (see the bottom panel of Figure 12). This fact has also been noted by Ciolfi & Siegel (2015b) based on a simplified analysis. As $t_{\text{diff,n}}$

varies only slightly across the different collapse times considered here (cf. upper panel of Figure 12), the plateau durations are remarkably similar ($\sim 10^5$ s; cf. the bottom panel of Figure 12). Moreover, the absolute luminosity levels $L_{\text{obs,tot}}$ during the second plateau phase are also very similar. This is because the total luminosity during this phase is essentially determined by the ratio of the internal energy of the nebula E_{nth} (which is very similar among the different runs) and $t_{\text{diff,n}}$ (cf. Section 4.4 of Paper I).

It is important to note that the ejecta material cools down and that the maxima of the thermal spectra drift out of the XRT band on the timescales considered here. Therefore, after $t = t_{\text{coll}}$ the X-ray light curves $L_{\text{obs,XRT}}$ differ somewhat from the total luminosity $L_{\text{obs,tot}}$ (cf. the bottom panel in Figures 11 and 12). In particular, the second plateaus of the X-ray light curves are characterized by lower luminosity levels and shorter durations of the order of $\sim 10^4$ s. Furthermore, as the PWN becomes optically thin before $t = 10^5$ s (cf. also Figure 3), a short breakout of luminous, non-thermal radiation from the interior of the PWN becomes visible in the X-ray band shortly after the second plateau (cf. Figure 11). This breakout is only short-lived as further cooling of the nebula prevents such high X-ray luminosities soon after the onset. In the case of $f_{\text{coll}} = 0.1$, the PWN has even cooled down to such an extent that this transition to the optically thin regime of the PWN does not lead to appreciable X-ray luminosities at all.

Finally, we note that in the recently proposed time-reversal scenario (Ciolfi & Siegel 2015a, 2015b), the X-ray light curves depicted in the lower panel of Figure 11 correspond to the observable X-ray afterglow of the SGRB as seen in the XRT band. We note that the two-plateau structure found here is remarkably similar to the structure of X-ray afterglows observed in a number of SGRB events (e.g., Gompertz et al. 2014). Furthermore, as the prompt SGRB emission is associated with the collapse of the NS in the time-reversal scenario, the X-ray emission predicted by our model prior to the collapse (as, e.g., depicted in the upper panel of Figure 11) corresponds to a precursor signal that can be searched for by future X-ray missions. If found, it would constitute a remarkable piece of evidence in favor of the time-reversal scenario. The essence of “time reversal” in this scenario is nicely illustrated by Figures 11 and 12: the energy radiated away from the system after $t = t_{\text{coll}}$ has been extracted from the NS prior to the collapse. This energy diffuses outward on the respective diffusion timescales and produces a characteristic two-plateau structured X-ray light curve.

5.2.2. Collapse During Phase I

In this section, we return to the problem of predicting the EM transient signal associated with an early collapse of the NS during Phase I. Such an early collapse is expected to occur either if the NS is hypermassive at birth or if it is supramassive but collapses due to (magneto-) hydrodynamic instabilities. In either case we numerically integrate the corresponding evolution equations (Equations (1)–(2) of Paper I) after the collapse as described in Section 4.4 of Paper I. In this case, the time of collapse, $t = t_{\text{coll}}$, is parametrized in units of t_{dr} , f_{coll} , $\text{PI} = t_{\text{coll}}/t_{\text{dr}}$.

Figure 13 shows X-ray light curves of radiation in the XRT band (cf. Section 2) for the fiducial parameter setup varying the time of collapse, σ_M , and κ . These are the most influential parameters concerning this early collapse scenario. At $t = t_{\text{coll}}$

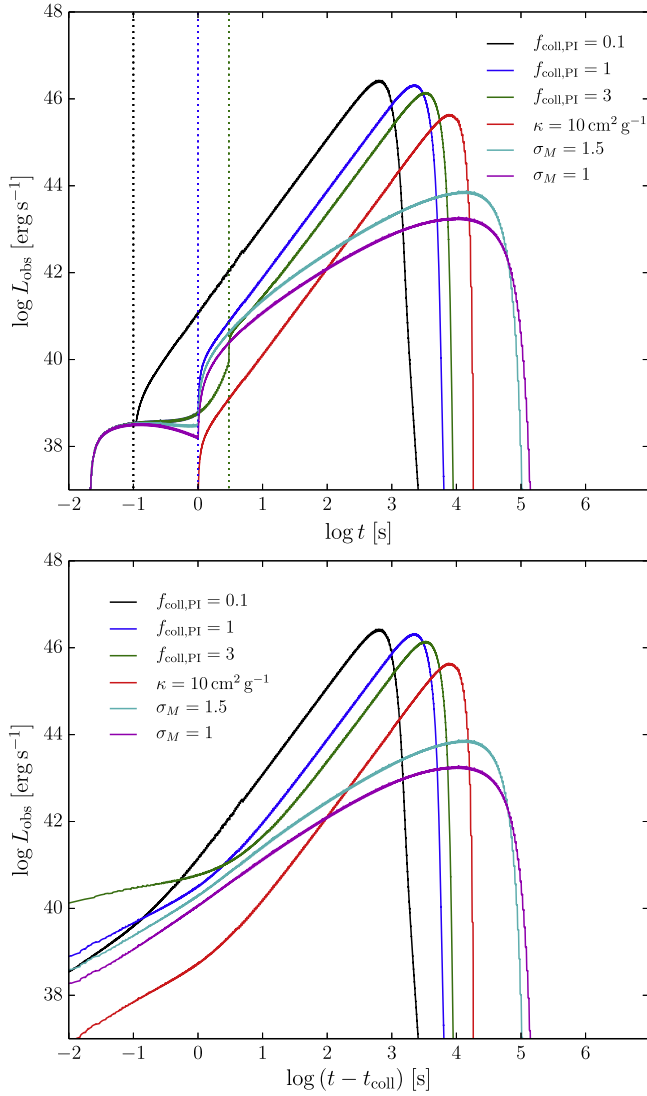


Figure 13. Early collapse of the NS during Phase I. Top: X-ray luminosity $L_{\text{obs, XRT}}$ (cf. Section 2) as seen by a remote observer for the fiducial parameter setup (cf. Table 1), but different values of $f_{\text{coll,PI}} = t_{\text{coll}}/t_{\text{dr}}$, σ_M , and κ . Dashed lines indicate the different times of collapse t_{coll} . Bottom: same light curves, but plotted as a function of the time after the respective collapse.

mass ejection from the NS suddenly stops and the ejected material starts to form a spherical shell of thickness $R_{\text{ej}} - R_{\text{in}}$ (cf. Section 4.1.2 of Paper I) that moves outward with a constant head speed $v_{\text{ej,in}}$ (see Figure 14). After $t = t_{\text{coll}}$ the total luminosity $L_{\text{obs,tot}}$ typically increases as a power law in time⁷ up to a maximum at a timescale $\sim 10^3 - 10^4$ s after the BNS merger. For the fiducial setup (cf. Table 1), the shell thickness remains constant (since $\sigma_v = 0$; cf. Section 4.1.1 of Paper I) and the peak emission frequency remains in the XRT band until late times. This is why the corresponding X-ray light curves show this power-law behavior and follow the total luminosity until shortly after the global maximum (cf. the $f_{\text{coll,PI}} = 0.1, 1, 3$ curves in Figure 13). When $\sigma_M < 2$, $\sigma_v > 0$ and the shell thickness increases $\propto t$. Hence, the temperature decreases more rapidly and the corresponding X-ray light curves deviate from a power-law increase soon after $t = t_{\text{coll}}$ as the peak emission

⁷ As both R_{ej} and R_{in} scale linearly with time, all other quantities show power-law behavior as well.

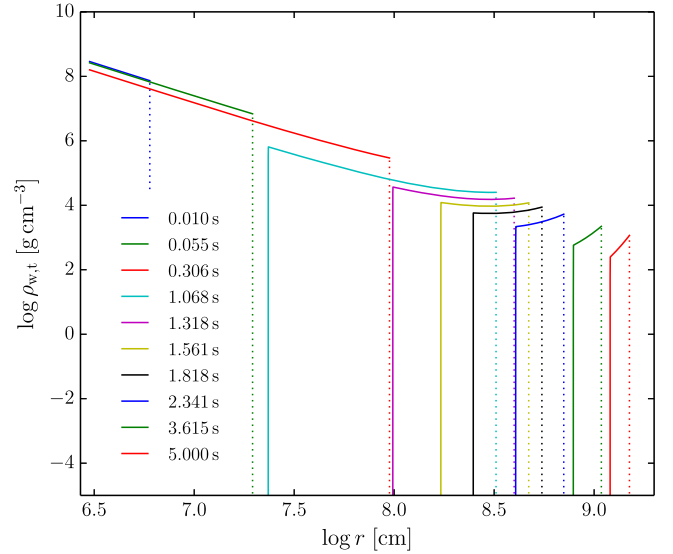


Figure 14. Snapshots of the density profiles of the baryon-loaded wind for selected times (fiducial parameter setup with $t_{\text{coll}} = 1$ s, cf. Table 1; cf. also Sections 4.4 and 4.1.1 of Paper I). After $t = t_{\text{coll}}$ the wind forms a spherical shell.

frequency moves out of the XRT band (cf. the $\sigma_M = 1, 1.5$ cases in Figure 13). Finally, we note that the higher opacity of $\kappa = 10 \text{ cm}^2 \text{ g}^{-1}$ leads to an overall dimmer light curve, with the power-law increase and global maximum being shifted to larger timescales.

In this early-collapse scenario, the maximum of the light curve is always followed by a monotonic and abrupt decrease in contrast to the typical (two-)plateau morphology found in the case of a collapse during Phase III. This is due to the absence of a PWN, which could further supply the ejecta matter with energy once the energy reservoir has been depleted.

6. LIGHT CURVE MORPHOLOGIES

After having discussed the influence of individual model parameters on the X-ray light curves in the previous section, we now explore the entire parameter space and classify the resulting light curves according to their morphology into different categories. For each of these categories, we show a few representative examples (see Figures 15 and 16) and point to some candidate SGRBs⁸ that are potentially consistent with the respective morphology. This division into categories is somewhat arbitrary and it is not necessarily exhaustive. We stress that a comparison with observational data is only intended to be on a qualitative level at the present stage. Fitting observational data with our model will be the subject of future work. Overall, we also distinguish between the standard scenario in which the SGRB itself is associated with the time of merger of the BNS system and the time-reversal scenario (Ciolfi & Siegel 2015a, 2015b) in which the SGRB is associated with the collapse of the remnant NS. In both cases, the light curves shown in Figures 15 and 16 correspond to the X-ray afterglows as seen in the XRT band of the *Swift* satellite. General issues regarding, e.g., the thermal/non-thermal nature of the spectra and late-time power-law decays observed in some SGRBs are discussed in Section 7.

⁸ XRT data of all SGRB events mentioned in this paper are available at http://www.swift.ac.uk/xrt_curves/.

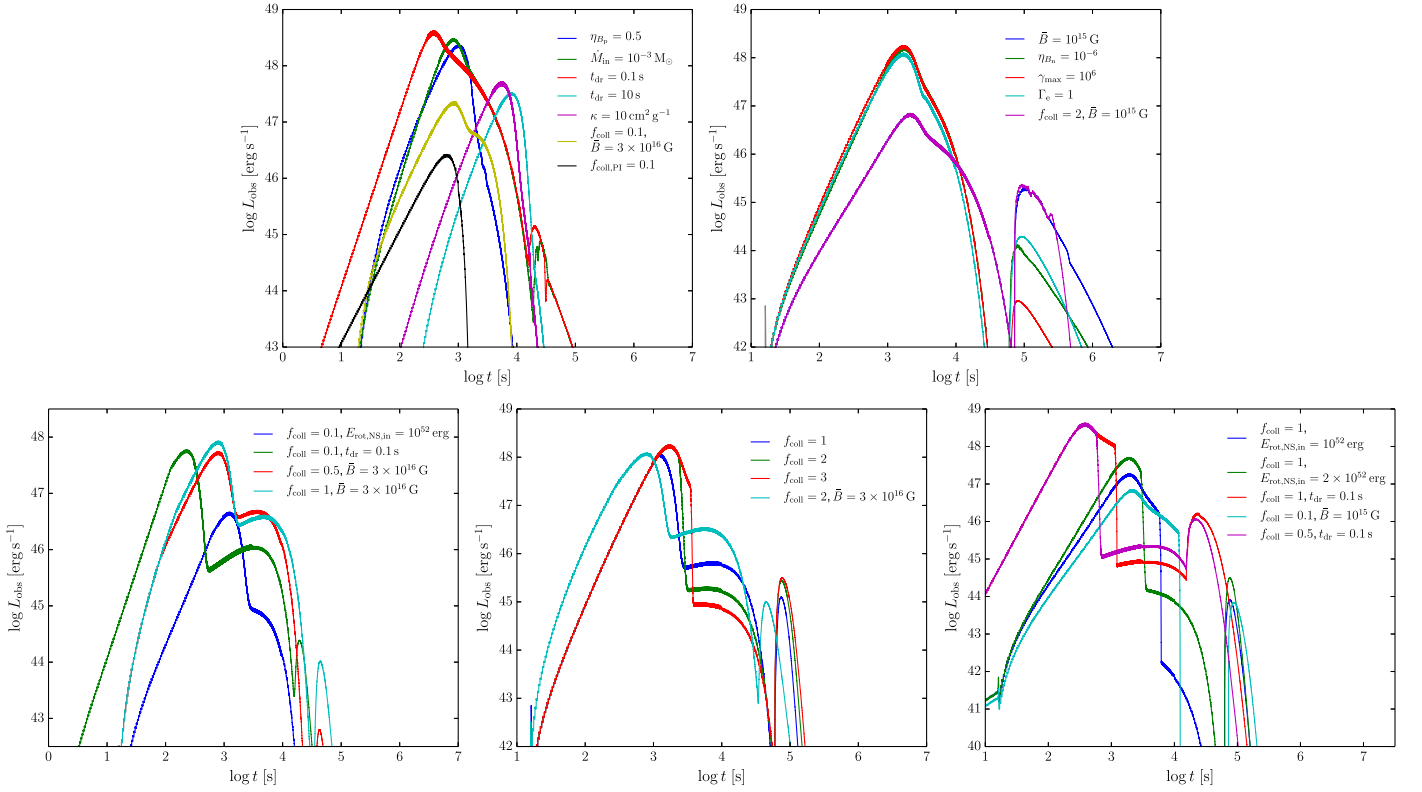


Figure 15. X-ray light curve morphologies (standard scenario). Upper row (left to right): single-maximum light curves with steep decay (M), single-maximum light curves with secondary maximum due to non-thermal radiation at late times (MM). Bottom row (left to right): plateau light curves (P), plateau light curves with a late-time flare of non-thermal radiation (PF), light curves with a late-time flare of non-thermal radiation showing absence of strong X-ray radiation at intermediate times (GF). All parameters are as in the fiducial setup (cf. Table 1), except for the ones specified in the respective legend.

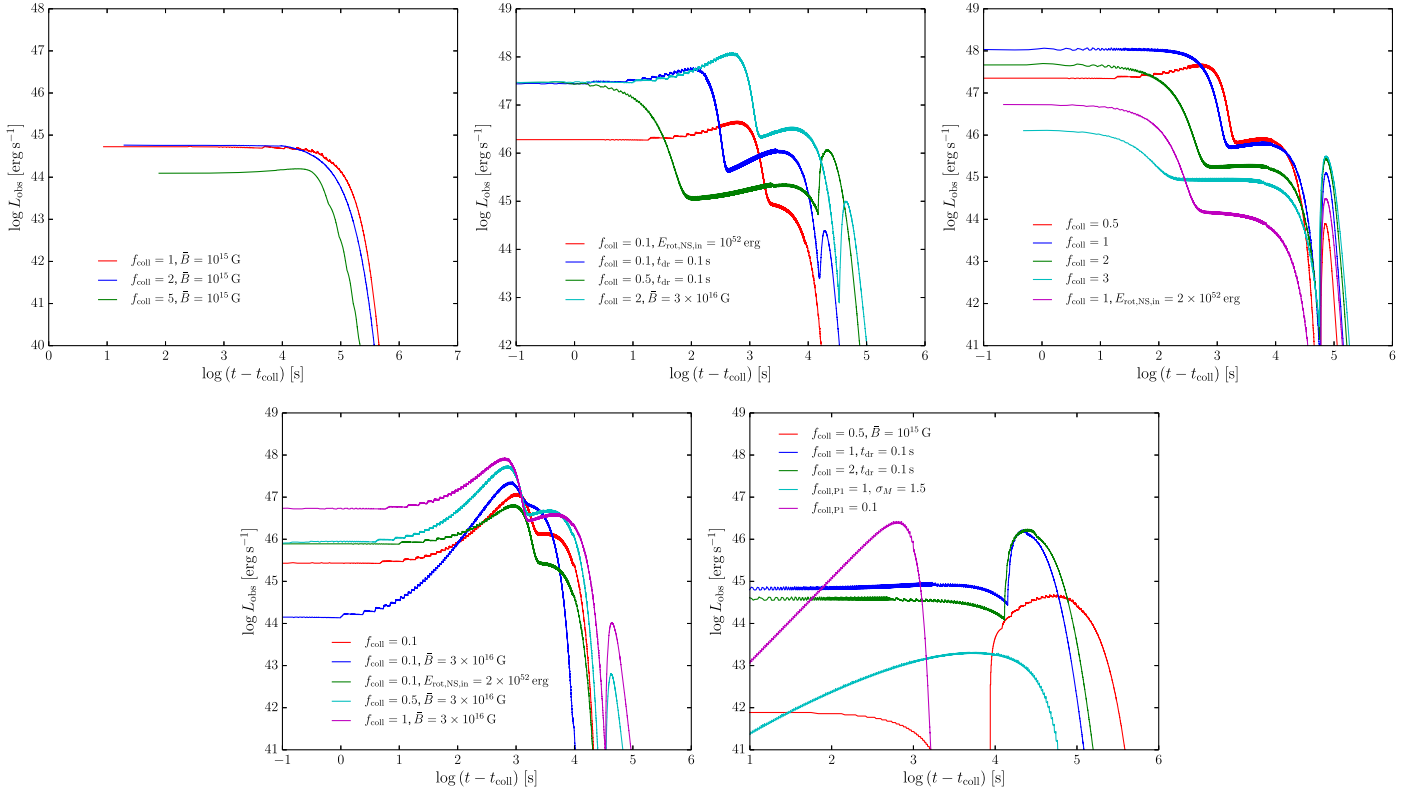


Figure 16. X-ray light curve morphologies (time-reversal scenario). Upper row (left to right): single-plateau light curves (SP), two-plateau light curves (TP), two-plateau light curves with a late-time flare (TPF). Bottom row (left to right): light curves with a rising plateau and abrupt decay (RP), light curves without (dominant/clear) plateaus (NP). All parameters are as in the fiducial setup (cf. Table 1), except for the ones specified in the respective legend.

6.1. Standard Scenario

Figure 15 shows five different categories of X-ray light curve morphologies, which we briefly discuss below. In contrast to the time-reversal case (Section 6.2), these light curves are characterized by a “delayed onset”: it typically takes $\sim 1\text{--}10$ s after the SGRB to reach appreciable X-ray luminosities of the order of $\gtrsim 10^{42}$ erg. This is mainly due to the very high optical depths of the ejecta matter at early times (cf. Section 4.1). The time of peak brightness is typically reached between $\sim 10^2$ and 10^4 s after the SGRB with luminosities of $\sim 10^{46}\text{--}10^{49}$ erg s $^{-1}$.

Cat. M—These light curves show a single maximum followed by a steep decay (upper left panel of Figure 15). They correspond to thermal radiation from the ejecta shell, with a non-thermal “tail” of radiation from the nebula at late times in some cases (cf. $t_{\text{dr}} = 0.1$ and $\dot{M}_{\text{in}} = 10^{-3} M_{\odot}$). Because of the single maximum and abrupt decay these light curves are qualitatively similar to the shapes of the observed X-ray afterglows of, e.g., GRB 080905A, GRB 090515, GRB 090607, GRB 100117A.

Cat. MM—These light curves show a global maximum due to thermal radiation from the ejecta shell, followed by a steep decay and a separated second “bump” of non-thermal radiation from the nebula (upper right panel of Figure 15). The non-thermal radiation typically decreases as a power law $\propto t^{-a}$, where $a \gtrsim 2$. This could explain some more moderate declines of X-ray luminosity at late times in some observed cases. Characteristic of these light curves is also the absence of high X-ray luminosity at intermediate times. Potential candidates for such a morphology could be, e.g., GRB 051227, GRB 061201, GRB 060313, GRB 070724A, GRB 071227, GRB 110112A, GRB 121226A, GRB 131004A. Furthermore, regarding timescales and luminosity levels, the second maximum of non-thermal radiation is consistent with the late-time X-ray rebrightening observed in some SGRB events, such as GRB 050724, GRB 080503, and the r-process powered kilonova candidate GRB 130603B (Grupe et al. 2006; Perley et al. 2009; Fong et al. 2014). Based on their models, Metzger & Piro 2014 and Gao et al. 2015 argued that such a rebrightening for GRB 080503 and GRB 130603B could be caused by radiation from a stable magnetar surrounded by a PWN (similar to our setup here) and thus called those GRBs candidate events for a “magnetar driven transient” or “magnetar-driven merger-novae.” We note that, in particular, Fong et al. (2014) reported a late-time ($t \gtrsim \text{day}$) X-ray excess of $L \simeq 4 \times 10^{43} (t/\text{day})^{\alpha}$ erg s $^{-1}$ for GRB 130603B, where $\alpha = -1.88 \pm 0.15$. As noted above, some of our light curves also show a power-law behavior with an exponent close to -2 . Furthermore, the timescales and luminosity levels of some of our models are consistent with such an X-ray excess at late times.

Cat. P—These light curves are characterized by a global maximum (as in the previous cases), followed by a plateau that is caused by the collapse of the NS (cf. Section 5.2.1) and a final steep decay (lower left panel of Figure 15). The radiation originates from the ejecta shell throughout the evolution and is thus thermal. The plateaus typically extend up to $\sim 10^4$ s and the luminosity levels are typically roughly two orders of magnitude lower than the preceding peak at $\sim 10^2\text{--}10^3$ s. This morphology together with the timescales and luminosity levels seems to resemble some of the SGRBs considered by Gompertz et al. (2013, 2014). More specifically, potential candidates for such a

morphology could be, e.g., GRB 051227, GRB 070714B, GRB 070724A, GRB 071227, GRB 080123, GRB 111121A.

Cat. PF—These X-ray afterglow light curves are very similar to Cat. P, except for the fact that there is a noticeable flare-like event of non-thermal radiation from the nebula after the plateau (bottom row of Figure 15, middle panel). This is due to the fact that the ejecta shell becomes optically thin during the plateau phase of the total luminosity (cf. Section 5.2.1). A potential candidate for this morphology could be, e.g., GRB 050724, which shows a flare-like event just after the plateau phase. However, as such flares are not always well separated from the plateau itself, this morphology can also be confused with Cat. P in some cases. Therefore, some of the GRB candidates for Cat. P could also apply to this category and vice versa.

Cat. GF—These are more peculiar light curves shown in the lower right panel of Figure 15. They are similar to Cat. PF, but characterized by an abrupt decrease after the global maximum and by absence of strong X-ray radiation (a “gap”) at intermediate times. The final flare dominates the luminosity at intermediate times.

6.2. Time-reversal Scenario

Figure 16 depicts examples for five different X-ray afterglow light curve morphologies in the time-reversal scenario. In contrast to the standard scenario (cf. Section 6.1) and except for a few peculiar cases, these light curves typically do not show a delayed onset. They are rather marked by very high X-ray luminosities starting from the SGRB itself. This is because at the times of collapse, the system is typically already radiating at a very high luminosity level. We note that in the time-reversal scenario, the X-ray luminosity predicted by our model prior to the collapse as discussed in Sections 6.1 and 4 and 5 represents a precursor signal that can be searched for by future X-ray missions.

Cat. SP—These are X-ray light curves characterized by a single plateau lasting up to $10^4\text{--}10^5$ s, followed by a rather steep decay (upper left panel of Figure 16). The radiation is purely non-thermal in the cases shown (broad-band synchrotron plus inverse Compton, cf. Section 4.3), as the collapse of the NS occurs at late times when the ejecta shell is already optically thin. This type of morphology seems to resemble some of the X-ray plateaus discussed by Rowlinson et al. (2013). Potential candidates for this morphology could be, e.g., GRB 051221A, GRB 060313, GRB 061201, GRB 070809, GRB 090510, GRB 111020A, 130603B, GRB 140903A. Some of these cases require a contribution from the standard X-ray afterglow of the SGRB jet itself in combination with our prediction (see Rowlinson et al. 2013 and Section 7).

Cat. TP—Together with Cat. TPF this family of light curves represents the most typical prototype for the time-reversal scenario, as it shows the characteristic two-plateau morphology (see Section 5.2.1; middle panel of the upper row in Figure 16). The plateau durations are determined by the photon diffusion times of the ejecta shell and the PWN (see Section 5.2.1). The luminosity levels and plateau durations of typically $\sim 1\text{--}10^3$ s and $\sim 10^3\text{--}10^4$ s for the first and the second plateau, respectively, are in very good agreement with some of the observed two-plateau structures discussed by Gompertz et al. (2014). Potential candidates for this morphology are GRB 051227, GRB 060614, GRB 070714B, GRB 070724A, GRB 071227, GRB 080123, GRB 111121A.

Cat. TPF—Same as *Cat. TP*, but with a late-time “flare” of non-thermal radiation from the nebula as the ejecta shell becomes optically thin (upper right panel of Figure 16). A potential candidate for this morphology is GRB 050724, which shows such a flare at late times attached to the second plateau (cf. Gompertz et al. 2014). However, as these flares are typically not well separated from the second plateau, many of such events could be confused with *Cat. TP* and some of the GRB candidates mentioned there could also apply to this category and vice versa.

Cat. RP—This family of light curves essentially shows a single plateau, but with a rising luminosity level (lower left panel of Figure 16). After the maximum there is a very short second “plateau” up to typically $\sim 10^3$ – 10^4 s, followed by a steep decay. The radiation is thermal throughout. Candidate SGRBs for this category could be, e.g., GRB 070714A, GRB 090607, GRB 131004A.

Cat. NP—These light curves are again more peculiar examples without a (dominant/characteristic) plateau (lower right panel of Figure 16). This family is rather marked by a single maximum or “bump” of thermal or purely non-thermal radiation. A maximum at early times $\lesssim 10^3$ s (as in the case of a collapse during Phase I; cf. the magenta curve and Section 5.2.2) is typically characterized by thermal radiation and could resemble some of the candidate GRBs noted in *Cat. M* of Section 6.1. The other light curves with maxima at later times ($\sim 10^4$ – 10^5 s) are either thermal (cyan curve; collapse during Phase I) or non-thermal (remaining curves; collapse during Phase III). The absence of strong X-ray radiation at early times in these cases is either due to a high optical depth (collapse during Phase I) or a low temperature of the ejecta material (collapse during Phase III). These late-time maxima could be consistent with the afterglow rebrightening observed in some SGRBs, such as GRB 050724, GRB 080503, and the r-process powered kilonova candidate GRB 130603B (Grupe et al. 2006; Perley et al. 2009; Fong et al. 2014; see also the discussion of *Cat. MM* in Section 6.1). The timescales for rebrightening in the aforementioned cases of $\sim 10^4$ – 10^5 s are in good agreement with the timescales for maximum brightness found here. This rebrightening is to be understood as an additional component to the fading standard X-ray afterglow of the SGRB jet itself, as the early X-ray emission in the aforementioned cases cannot be explained by the light curves such as those in the lower right panel of Figure 16. Such an interpretation is similar to Metzger & Piro (2014) and Gao et al. (2015), who, according to their models, noted that the observed X-ray excess at late times in some of the aforementioned cases can be consistent with a magnetar driven transient (or “merger-nova”) in addition to the standard X-ray afterglow.

7. DISCUSSION AND CONCLUSION

In this paper, we have presented X-ray light curves and spectra originating from the post-merger evolution of a BNS system, based on our model proposed in the companion paper (Paper I). Given initial data that can be read off from numerical relativity simulations of the merger and early post-merger process, this model provides a self-consistent evolution of the system over much longer time and length scales inaccessible to those simulations. It thus bridges the gap between such simulations and the timescales relevant for observations of SGRB afterglows with satellite missions like *Swift*.

Baryon pollution—Our model is based on the notion that a long-lived NS is formed in a large fraction of BNS merger events, which is either hypermassive, supramassive, or stable. As we have argued (see Paper I), a generic feature of such a newly formed object is strong baryon pollution in its surrounding due to mass ejected dynamically during and shortly (\sim ms) after the merger (e.g., Oechslin et al. 2007; Bauswein et al. 2013; Hotokezaka et al. 2013; Kastaun & Galeazzi 2015) and subsequent neutrino-driven and magnetically induced winds on longer timescales from the remnant NS itself and from a potential accretion disk (e.g., Dessart et al. 2009; Metzger & Fernández 2014; Siegel et al. 2014). As we have shown, these ejecta create an optically thick environment which traps radiation on timescales of interest, even for total ejecta masses as small as $M_{\text{ej}} \sim 5 \times 10^{-4} M_{\odot}$. This is in contrast to typical “magnetar models” for SGRBs (e.g., Gompertz et al. 2013, 2014; Rowlinson et al. 2013; Lü et al. 2015), which assume an optically thin environment such that the spin-down energy of the newly formed magnetar after the merger could immediately and directly be converted into X-ray radiation, $L_{\text{X}}(t) \propto L_{\text{sd}}(t)$ (by some yet to be specified process).

General properties of the X-ray signal—One important consequence of our approach, which takes such baryon pollution into account, is a “delayed onset” of radiation from the post-merger system at ~ 1 – 10 s after merger. This is an intrinsic feature of baryon pollution that will be present even if further potential sources for EM radiation not considered here are included.⁹ The radiation typically peaks at $\sim 10^2$ – 10^4 s after merger in the X-ray band with luminosities of $\sim 10^{46}$ – 10^{49} erg s⁻¹. Scanning the whole parameter space (cf. Table 1) we find that these timescales and luminosities are a robust prediction of the model, even when considering uncertainties in the opacity of the ejecta material (cf. Sections 3.1 and 5.1). These ranges are unlikely to change even if a more detailed computation of opacities including bound-free absorption due to only partial ionization of the material was attempted. However, further acceleration of the ejected material in Phase III (not considered here) may shift the times of maximum brightening to somewhat earlier times (see below).

Electromagnetic counterpart to GW—We note that according to our model, such a transient X-ray signal is isotropic and it is expected for all BNS mergers that lead to the formation of a long-lived (\gtrsim tens ms) remnant NS, regardless of whether it is hypermassive, supramassive, or stable. As we have pointed out (cf. Section 1 of Paper I), the fraction of such BNS mergers should be very high, such that we can write the rate of these X-ray transients r_{X} in terms of the rate of BNS mergers r_{BNS} as

$$r_{\text{X}} = f_{\text{NS}} r_{\text{BNS}}, \quad (5)$$

where f_{NS} can be at least of the order of a few tens of percent. This transient is also orders of magnitude more luminous than other quasi-isotropic EM transients expected to result from a BNS merger, such as r-process powered kilonovae (or “macronovae”), which are thought to emit mostly in the IR to UV with typical luminosities of $L \sim 10^{41}$ – 10^{42} erg s⁻¹ (e.g., Li & Paczyński 1998; Kulkarni 2005; Metzger et al. 2010; Piran et al. 2013). We note again that in contrast to such kilonovae, the X-ray transient found here would be a

⁹ Additional sources of energy could be the gravitational, thermal, and EM energy of a short-lived accretion disk that might form around the remnant NS.

clear sign of a long-lived NS and would thus distinguish between a BNS and an NS–BH merger. In contrast to these isotropic signals, the prompt SGRB radiation itself (if associated with a BNS merger) is thought to be collimated and will thus be beamed away from the observer in a large fraction $1 - f_{\text{beam}} = \cos \theta_{\text{jet}}$ of events, where θ_{jet} denotes the beaming angle of the jet (see Berger 2014 for an overview of observations to date). Furthermore, the rate of potentially observable SGRBs,

$$r_{\text{SGRB}} = f_{\text{beam}} f_{\text{jet}} r_{\text{BNS}}, \quad (6)$$

is further reduced by a factor f_{jet} with respect to the BNS merger rate r_{BNS} , since not all BNS mergers may generate a jet to produce a SGRB. For instance, baryon pollution as described above can choke jets (e.g., Murguía-Berthier et al. 2014; Nagakura et al. 2014) and it seriously threatens the formation of a highly relativistic outflow at or shortly after the time of merger. The combined product of the efficiency factors is constrained to be

$$f_{\text{beam}} f_{\text{jet}} \lesssim 0.3\% \quad (7)$$

if the likely local BNS merger rate of $\sim 10^{-6} \text{ Mpc}^{-3} \text{ yr}^{-1}$ (cf. Abadie et al. 2010 and references therein)¹⁰ is to be reconciled with the local SGRB rate of $\sim 3 \times 10^{-9} \text{ Mpc}^{-3} \text{ yr}^{-1}$ (Wanderman & Piran 2015 and references therein; cf. also Metzger & Berger 2012).¹¹ In particular, we note that to date no SGRB event with known redshift has been observed within the local sensitivity volume of the advanced LIGO/Virgo GW detector network. Hence, for coincident EM and GW observations of BNS mergers it is desirable to identify bright isotropic EM counterparts that are formed in a high fraction of events. Furthermore, the timescales for generating early-warning triggers for EM follow-up observations of the GW signal is rather challenging in the case of the SGRB itself (Cannon et al. 2012). During the first generation of ground-based laser interferometers such alerts were sent out with typical latencies of 10–30 minutes (Cannon et al. 2012; Evans et al. 2012). This is far too long compared to the time frame of at most 1–2 s to catch the prompt SGRB emission (assuming that the SGRB is produced at the time of merger, see below). While parts of this latency can, in principle, be significantly reduced for the advanced LIGO/Virgo setup (Cannon et al. 2012), sending out alerts to search for the SGRB prompt emission still remains a challenge. However, given a timescale for maximum brightness of $\sim 10^2\text{--}10^4$ s, even the latency of the first generation warning system should provide a realistic chance to search for the X-ray transient predicted by our model. Hence, the first advanced LIGO/Virgo observing runs starting in 2015 should be able to trigger EM follow-up observations to search for such X-ray transients. If found, such an observation would represent a clear indication in favor of our model. At the same time it would provide strong evidence for the association of the GW

observation with a BNS merger (and not, e.g., an NS–BH binary merger) and thus confirm the astrophysical origin of the GW signal. In conclusion, all criteria mentioned in Section 1 are met: the high luminosity, its isotropy, the long duration, the high fraction of events, its ability to identify a BNS merger, and, additionally, a realistic timescale for triggering EM follow-up make the X-ray transient predicted by our model an ideal EM counterpart to the GW signal of the final inspiral and merger of a BNS system.

X-ray light curve morphologies and SGRBs—X-ray light curves arising from the present model have been discussed and classified according to their morphology (cf. Figures 15 and 16), both in the standard and the time-reversal scenario for SGRBs (prompt burst associated with the time of merger or with the time of collapse of the merger remnant). As a reference energy range we have employed the *Swift* XRT band. There is a wide spectrum of different morphologies for both scenarios, although the variety is somewhat richer in the time-reversal case. This can be a useful property if a single model is to explain the observed wide variety of X-ray afterglow light curves. In particular, our model is able to explain single and two-plateau shaped light curves (cf. Cat. SP, TP, P) as, e.g., reported by Rowlinson et al. (2013), Gompertz et al. (2013, 2014), and Lü et al. (2015), with additional late-time flares in some cases (cf. Cat. PF and TPF). The timescales for such plateaus are given by the photon diffusion time of the ejecta envelope and the PWN. We find that the timescales ($\sim 1\text{--}10^3$ s for a first and $\sim 10^3\text{--}10^4$ s for a second/single plateau) and luminosity levels ($\sim 10^{44}\text{--}10^{49} \text{ erg s}^{-1}$) for such plateaus are in excellent agreement with observations. Moreover, there are categories showing a late-time rebrightening of the X-ray emission (cf. Cat. MM and NP) similar to some observed cases (GRB 050724, GRB 080503, GRB 130603B; Grupe et al. 2006; Perley et al. 2009; Fong et al. 2014; Metzger & Piro 2014; Gao et al. 2015). Again, the timescales and possible luminosity levels are broadly consistent with these observations at late times. Many categories show light curves with rather steep decays, which are due either to the ejecta material cooling down and the peak energy of the spectrum moving out of the XRT band or the PWN cooling down and consuming its residual energy. Steep decays in X-ray light curves were previously interpreted as a collapse of the remnant NS to a black hole (e.g., Rowlinson et al. 2010, 2013). While our model allows for such steep decays of the X-ray light curve, there might be problems in explaining power-law decays with moderate slopes at late times. There are a few observational cases that potentially challenge our model in this regard; some of the events classified as “external plateaus” by Lü et al. (2015), which are consistent with a late-time temporal index of -1 after a plateau phase, might belong to this category. However, as the steepness of these decays is somewhat dependent on the radiation transport and the cooling model (see, e.g., Section 4.4 of Paper I), a more detailed implementation of the thermal and non-thermal emission in our model might resolve this issue (see below). Furthermore, we note that we have pointed out a few characteristic observational examples for the respective X-ray light curve morphologies in Section 6. As a general note of caution, we stress that the present comparison with observational data is only based on timescales and overall luminosity levels and thus remains rather on a qualitative level. Routinely fitting observational data by

¹⁰ As BNS merger rates for the local universe are uncertain, we take here the “realistic estimate” of Abadie et al. (2010).

¹¹ Recent estimates for the current event rate of SGRBs essentially range within $(1\text{--}10) \times 10^{-9} \text{ Mpc}^{-3} \text{ yr}^{-1}$ (cf. Table 4 of Wanderman & Piran 2015 and references given there; we have chosen a representative value of $3 \times 10^{-9} \text{ Mpc}^{-3} \text{ yr}^{-1}$).

employing our model is beyond the scope of the present paper, but will be attempted in future work.

Additional components to the X-ray light curve—The (X-ray) afterglow light curves predicted by our model represent the intrinsic contribution from the post-merger system composed of an NS (or a black hole after collapse), its PWN, and the confining ejecta envelope. They do not include the X-ray signature of the prompt emission and a fading tail. An early steep-decay component superimposed to our X-ray light curves might be needed to explain the observed X-ray light curves of some SGRB events (cf. also Rowlinson et al. 2013). This initial steep decay can represent a gradual decline of the X-ray emission from the prompt burst itself. It can also be due to the high-latitude effect if the prompt emission is “switched off” abruptly (Kumar & Panaitescu 2000; Kumar & Zhang 2015). The latter phenomenon is essentially a time-of-flight effect due to photons from different portions of the jet arriving slightly retarded, depending on the angle with respect to the observer direction. It fades out the prompt emission as $\propto t^{-\alpha}$, where $\alpha = \beta + 2$, with β the spectral index of the prompt emission.

SGRBs with extended emission (EE)—Lü et al. (2015) have recently argued that SGRBs with EE in the BAT band correspond to the same phenomenon as SGRBs with an early plateau phase in the XRT band, and that the detection of such early plateaus by BAT is just an instrumental selection effect depending on brightness. EE in the context of the magnetar scenario has been interpreted as dissipation of kinetic energy of an early modestly magnetized, neutrino-heated magnetar wind in internal shocks that give rise to synchrotron radiation (Metzger et al. 2008), as the breakout of a magnetic jet through the ejecta envelope of a PWN (Bucciantini et al. 2012), as mass ejection via magnetic propelling of an accretion disk around the remnant NS (Gompertz et al. 2014), or as magnetar wind leaking out from the surrounding ejecta through a hole drilled out by the SGRB jet (Gao et al. 2015). We note that in the model presented here, such early X-ray plateaus and the typical two-plateau structure evident in SGRBs with EE (Gompertz et al. 2014) are naturally explained in terms of photon diffusion through the ejecta matter and the PWN (see Cat. P, PF, TP, TPF in Section 6 and Section 5.2.1). This does not exclude a possible further contribution from magnetar wind leaking out from the ejecta through the jet hole as suggested by Gao et al. (2015). However, such a component would only be visible along the jet direction, while the radiation forming the early plateaus in our model is, in general, isotropic.

Time-reversal scenario—The model presented here can accommodate the recently proposed time-reversal scenario for SGRBs (Ciolfi & Siegel 2015a, 2015b), in which the SGRB is associated with the collapse of the remnant NS. Detailed modeling in the present paper quantitatively confirms the estimates for the photon diffusion timescale of the nebula and the ejecta shell and thus the duration of the X-ray afterglows obtained earlier (Ciolfi & Siegel 2015b). Here, we have reported for the first time detailed computations for the X-ray afterglow light curves in this scenario, which show a wide range of morphologies. In particular, this scenario gives rise to two-plateau structures with plateau durations and luminosity levels compatible with observations (see above). Additionally, the present study predicts light curves for the X-ray radiation preceding the prompt SGRB emission within this scenario. Such emission corresponds to the part of the X-ray light curve prior to the collapse of the NS, which is characterized by a

delayed onset after the BNS merger, reaching a maximum brightness of $\sim 10^{46} - 10^{49}$ erg s $^{-1}$ at a timescale of minutes to hours after merger (see above). There can be additional features not included in the light curve modeling here, such as a short duration, strong non-thermal signal from the shock front as it reaches the ejecta surface at the end of Phase II, and possible flare-like irregularities as the SGRB jet drills through the ejecta envelope. Such features could explain observed precursors to the prompt SGRB emission as early as ~ 100 s before or as close as a fraction of a second to the onset of the main burst (Troja et al. 2010). The light curve calculations presented here provide clear predictions for strong X-ray emission prior to the SGRB that can be searched for by wide-field X-ray telescopes. If found, it would represent smoking-gun evidence for the time-reversal scenario. As detailed above, the timescales of the delayed onset makes the search for such isotropic X-ray radiation prior to the SGRB a feasible and exciting task for multi-messenger astronomy with joint GW and EM observations. An observational strategy including GW observations to trigger X-ray and γ -ray observations has thus the potential to confirm the association of SGRBs with BNS mergers, the time-reversal scenario, and the astrophysical origin of the GW signal at the same time. As the advanced LIGO/Virgo detector network is starting the first science runs in 2015, such EM follow-up campaigns become a very timely undertaking.

X-ray spectra—Our model predicts a characteristic transition from thermal to non-thermal emission during the post-merger evolution of the system (see Section 4.3). Only at late times when the ejecta shell has expanded far enough to become optically thin, genuine non-thermal radiation (mainly broadband synchrotron radiation) from the PWN is emitted toward the observer. Observationally, not much is known about the spectra of SGRB afterglows and their temporal evolution. It is generally assumed that they are of non-thermal nature, originating from synchrotron radiation of a power-law distribution of electrons. In the XRT band, spectra are typically fit by a power law with a time-dependent power-law index (cf., e.g., Rowlinson et al. 2013). In our model, we assign a single representative temperature to the ejecta shell, which reflects a high degree of idealization. However, instead of a single temperature and thus a pure Planck spectrum for the thermal radiation from the ejecta shell, the ejecta material will be characterized by spatial gradients in temperature. The actual emergent spectrum will thus be a superposition of individual Planck spectra of different effective temperatures that depending on the temperature gradient may combine to give a power-law spectrum in the XRT band, just as the individual synchrotron spectra of electrons following a power-law distribution in the Lorentz factor superpose to give a power-law spectrum. Moreover, as the ejecta material will be (at least partially) ionized, inverse Compton scattering of thermal photons off free electrons might create power-law-like high-energy tails for the individual Planck spectra. Nevertheless, as long as the effective temperature of the ejecta matter in our model resides within the XRT band, the overall X-ray spectra should still capture the main dynamical and energetical effects to reliably determine the X-ray light curve morphology. Due to an enhanced high-energy tail, a more detailed computation of the emergent spectrum could lead to less steep decays of the X-ray light curve as the ejecta is cooling down and the average temperature is moving out of the XRT band. This could resolve the aforementioned problem of describing more shallow decays

of the X-ray radiation, in particular at the end of a (second) plateau phase.

Future improvements—Our modeling of the X-ray light curves already reflects a high level of detail. Nevertheless, it is built on simplifying assumptions. More realistic X-ray spectra, their evolution and associated light curves require a more detailed spectral modeling of the thermal radiation from the ejecta shell as discussed above. Moreover, a time-dependent modeling of the radiative processes in the PWN is required to include effects of a non-zero albedo of the ejecta matter (Metzger & Piro 2014) and to consider further acceleration of the ejecta shell during Phase III. The latter aspect may somewhat influence the timescales of the X-ray light curves. Furthermore, such a time-dependent modeling of the radiative processes in the PWN would also provide a more accurate evolution of the PWN after the collapse and thus provide a more realistic spectral evolution of photons inside the PWN in the post-collapse phase. Finally, adding thermal Comptonization to the radiative interactions in the PWN is desirable, as it might affect the shape of the nebula X-ray spectrum. The main conclusions of this work are, however, unlikely to be affected by such future improvements.

We thank B. F. Schutz, W. Kastaun, B. D. Metzger, G. Ghirlanda, and M. G. Bernardini for valuable discussions. R. C. acknowledges support from MIUR FIR Grant No. RBFR13QJYF.

REFERENCES

- Abadie, J., Abbott, B. P., Abbott, R., et al. 2010, *CQGra*, **27**, 173001
- Accadia, T., Acernese, F., Antonucci, F., et al. 2011, *CQGra*, **28**, 114002
- Antoniadis, J., Freire, P. C. C., Wex, N., et al. 2013, *Sci*, **340**, 448
- Barnes, J., & Kasen, D. 2013, *ApJ*, **775**, 18
- Barthelmy, S. D., Chincarni, G., Burrows, D. N., et al. 2005a, *Natur*, **438**, 994
- Barthelmy, S. D., Barbier, L. M., Cummings, J. R., et al. 2005b, *SSRv*, **120**, 143
- Bauswein, A., Goriely, S., & Janka, H.-T. 2013, *ApJ*, **773**, 78
- Belczynski, K., O’Shaughnessy, R., Kalogera, V., et al. 2008, *ApJL*, **680**, L129
- Berger, E. 2014, *ARA&A*, **52**, 43
- Berger, E., Fong, W., & Chornock, R. 2013, *ApJL*, **774**, L23
- Bucciantini, N., Metzger, B. D., Thompson, T. A., & Quataert, E. 2012, *MNRAS*, **419**, 1537
- Bühler, R., & Blandford, R. 2014, *RPPh*, **77**, 066901
- Burrows, D. N., Hill, J. E., Nousek, J. A., et al. 2005, *SSRv*, **120**, 165
- Cannon, K., Cariou, R., Chapman, A., et al. 2012, *ApJ*, **748**, 136
- Ciolfi, R., & Siegel, D. M. 2015a, in *Proc. Swift: 10 Years of Discovery*, PoS (SWIFT 10), ed. P. Caraveo, P. D’Avanzo, N. Gehrels, & G. Tagliaferri (Trieste, Italy: Proc. Science, SISSA), 108
- Ciolfi, R., & Siegel, D. M. 2015b, *ApJL*, **798**, L36
- Demorest, P. B., Pennucci, T., Ransom, S. M., Roberts, M. S. E., & Hessels, J. W. T. 2010, *Natur*, **467**, 1081
- Dessart, L., Ott, C. D., Burrows, A., Rosswog, S., & Livne, E. 2009, *ApJ*, **690**, 1681
- Eichler, D., Livio, M., Piran, T., & Schramm, D. N. 1989, *Natur*, **340**, 126
- Evans, P. A., Fridriksson, J. K., Gehrels, N., et al. 2012, *ApJS*, **203**, 28
- Fong, W., Berger, E., Metzger, B. D., et al. 2014, *ApJ*, **780**, 118
- Fox, D. B., Frail, D. A., Price, P. A., et al. 2005, *Natur*, **437**, 845
- Gao, H., Ding, X., Wu, X.-F., Dai, Z.-G., & Zhang, B. 2015, *ApJ*, **807**, 163
- Gehrels, N., Chincarini, G., & Giommi, P. 2004, *ApJ*, **611**, 1005
- Gehrels, N., Sarazin, C. L., O’Brien, P. T., et al. 2005, *Natur*, **437**, 851
- Giacomazzo, B., & Perna, R. 2013, *ApJL*, **771**, L26
- Gompertz, B. P., O’Brien, P. T., & Wynn, G. A. 2014, *MNRAS*, **438**, 240
- Gompertz, B. P., O’Brien, P. T., Wynn, G. A., & Rowlinson, A. 2013, *MNRAS*, **431**, 1745
- Grupe, D., Burrows, D. N., Patel, S. K., et al. 2006, *ApJ*, **653**, 462
- Harry, G. M., & LIGO Collaboration 2010, *CQGra*, **27**, 084006
- Hotokezaka, K., Kyutoku, K., Tanaka, M., et al. 2013, *ApJL*, **778**, L16
- Janka, H.-T., Eberl, T., Ruffert, M., & Fryer, C. L. 1999, *ApJL*, **527**, L39
- Kasen, D., Badnell, N. R., & Barnes, J. 2013, *ApJ*, **774**, 25
- Kastaun, W., & Galeazzi, F. 2015, *PhRvD*, **91**, 064027
- Kennel, C. F., & Coroniti, F. V. 1984, *ApJ*, **283**, 694
- Kulkarni, S. R. 2005, arXiv:astro-ph/0510256
- Kumar, P., & Panaitescu, A. 2000, *ApJL*, **541**, L51
- Kumar, P., & Zhang, B. 2015, *PhR*, **561**, 1
- Lasota, J.-P., Haensel, P., & Abramowicz, M. A. 1996, *ApJ*, **456**, 300
- Li, L.-X., & Paczyński, B. 1998, *ApJL*, **507**, L59
- Lü, H.-J., Zhang, B., Lei, W.-H., Li, Y., & Lasky, P. D. 2015, *ApJ*, **805**, 89
- Margalit, B., Metzger, B. D., & Beloborodov, A. M. 2015, *PhRvL*, **115**, 171101
- Metzger, B. D., & Berger, E. 2012, *ApJ*, **746**, 48
- Metzger, B. D., & Fernández, R. 2014, *MNRAS*, **441**, 3444
- Metzger, B. D., & Piro, A. L. 2014, *MNRAS*, **439**, 3916
- Metzger, B. D., Quataert, E., & Thompson, T. A. 2008, *MNRAS*, **385**, 1455
- Metzger, B. D., Vurm, I., Hascoët, R., & Beloborodov, A. M. 2014, *MNRAS*, **437**, 703
- Metzger, B. D., Martínez-Pinedo, G., Darbha, S., et al. 2010, *MNRAS*, **406**, 2650
- Murguia-Berthier, A., Montes, G., Ramirez-Ruiz, E., De Colle, F., & Lee, W. H. 2014, *ApJL*, **788**, L8
- Nagakura, H., Hotokezaka, K., Sekiguchi, Y., Shibata, M., & Ioka, K. 2014, *ApJL*, **784**, L28
- Narayan, R., Paczynski, B., & Piran, T. 1992, *ApJL*, **395**, L83
- Oechslin, R., Janka, H.-T., & Marek, A. 2007, *A&A*, **467**, 395
- Olmi, B., Del Zanna, L., Amato, E., & Bucciantini, N. 2015, *MNRAS*, **449**, 3149
- Paczynski, B. 1986, *ApJL*, **308**, L43
- Paschalidis, V., Ruiz, M., & Shapiro, S. L. 2015, *ApJL*, **806**, L14
- Perley, D. A., Metzger, B. D., Granot, J., et al. 2009, *ApJ*, **696**, 1871
- Pinto, P. A., & Eastman, R. G. 2000, *ApJ*, **530**, 757
- Piran, T., Nakar, E., & Rosswog, S. 2013, *MNRAS*, **430**, 2121
- Rezzolla, L., Giacomazzo, B., Baiotti, L., et al. 2011, *ApJL*, **732**, L6
- Rezzolla, L., & Kumar, P. 2015, *ApJ*, **802**, 95
- Roberts, L. F., Kasen, D., Lee, W. H., & Ramirez-Ruiz, E. 2011, *ApJL*, **736**, L21
- Roming, P. W. A., Kennedy, T. E., Mason, K. O., et al. 2005, *SSRv*, **120**, 95
- Rosswog, S. 2005, *ApJ*, **634**, 1202
- Rowlinson, A., O’Brien, P. T., Metzger, B. D., Tanvir, N. R., & Levan, A. J. 2013, *MNRAS*, **430**, 1061
- Rowlinson, A., O’Brien, P. T., Tanvir, N. R., et al. 2010, *MNRAS*, **409**, 531
- Shapiro, S. L. 2000, *ApJ*, **544**, 397
- Shibata, M., Duez, M. D., Liu, Y. T., Shapiro, S. L., & Stephens, B. C. 2006, *PhRvL*, **96**, 031102
- Siegel, D. M., & Ciolfi, R. 2016, *ApJ*, **819**, 14
- Siegel, D. M., & Ciolfi, R. 2015a, in *Proc. Swift: 10 Years of Discovery*, PoS (SWIFT 10), ed. P. Caraveo, P. D’Avanzo, N. Gehrels, & G. Tagliaferri (Trieste, Italy: Proc. Science, SISSA), 169
- Siegel, D. M., Ciolfi, R., & Rezzolla, L. 2014, *ApJL*, **785**, L6
- Singer, L. P., Price, L. R., Farr, B., et al. 2014, *ApJ*, **795**, 105
- Tanaka, M., & Hotokezaka, K. 2013, *ApJ*, **775**, 113
- Tanaka, M., Hotokezaka, K., Kyutoku, K., et al. 2014, *ApJ*, **780**, 31
- Tanvir, N. R., Levan, A. J., Fruchter, A. S., et al. 2013, *Natur*, **500**, 547
- Troja, E., Rosswog, S., & Gehrels, N. 2010, *ApJ*, **723**, 1711
- Wanderman, D., & Piran, T. 2015, *MNRAS*, **448**, 3026
- Yang, B., Jin, Z.-P., Li, X., et al. 2015, *NatCo*, **6**, 7323 (nature.com/ncomms/2015/150611/ncomms8323/full/ncomms8323.html)
- Zhang, B., & Mészáros, P. 2001, *ApJL*, **552**, L35